1991

Optimization of DFB semiconductor laser diode optical response under ultra-high speed, large signal modulation

Thomas Francis Strelchun
Lehigh University

AUTHOR:Strelchun, Thomas Francis

TITLE:Optimization of DFB Semiconductor Laser Diode Optical Response under Ultra-High Speed...

DATE: January 1992

OPTIMIZATION OF DFB SEMICONDUCTOR LASER DIODE OPTICAL RESPONSE UNDER ULTRA-HIGH SPEED, LARGE SIGNAL MODULATION

by

Thomas Francis Strelchun

A Thesis

Presented to the Graduate Committee

of Lehigh University

in Candidacy for the Degree of

Master of Science

in

Electrical Engineering

Lehigh University

1991

This thesis is accepted and approved in partial fulfillment of the requirements for the degree of Master of Science in Electrical Engineering.

December 2, 1991
Date

Advisor in Charge

CSEE Department Chairperson

Table of Contents

LIST OF FIGURES

ABSTRACT

A limit to DFB semiconductor laser performance under high speed, large scale modulation in a lightwave communications system is quantified with respect to metrics including optical pulse extinction ratio (ER) and wavelength chirp. Through modeling, it is found that the optical ON power using conventional 5 Gbit modulation techniques is limited due to excessive ER to a ratio of the structure saturation power, P_{sat}, which is $P_{sat}/4$.

The laser carrier and photon density responses are modeled using a nonlinear form of optical gain saturation due to spectral hole burning via intra-band gain saturation. Furthermore, a method for computing the time averaged spectrum, taking into account the optical gain saturation is developed. Under large scale modulation, the total optical wavelength spectral width (TSW), consisting of transient and adiabatic contributions, increases sublinearly with increasing modulation frequency, asymptotically approaching the large adiabatic spectral width of a structure in complete gain saturation.

Additional modeling is used to shape the modulation current, within the boundaries of the nonlinear coupled photon and carrier density rate equations, in order to minimize the transient wavelength chirp contributions to the

TSW. A 37 % reduction in TSW , from 16.6 A to 10.4 A, is realized for a modeled device at 5 Gbits using shaped versus conventional square wave current modulation. A 60 % improvement is achieved for the ER at average optical power levels approaching 20 mW under large scale modulation using pulse shaping techniques.

The optical outputs of various 1.55 μm DFB lasers are analyzed in the time and time averaged wavelength spectral domains at 5 Gbits in an effort to explore the onset of gain saturation effects due to spectral hole burning. Observed wavelength chirp and optical pulse features are in good agreement with the modeling results.

I. Introduction

A phenomenon occurs in semiconductor lasers that limits the effectiveness of high speed, large scale modulation. This phenomenom is spectral hole burning, which is responsible for optical gain reduction at high optical output levels. Relaxation oscillations are dampened and optical pulse fall times are increased due to the reduction of optical gain during large scale, high speed modulation.

Normally, spectral hole burning reduction of optical gain is included in the laser carrier and photon rate equations as [1]

$$g = g_L(1- P/P_S) \qquad (1)$$

where

g_L -> modal gain at threshold

P -> facet output power

P_S -> saturation power

Depending on the device material and wavelength, P_S varies from 100 - 1000 mW. Equation 1 is considered valid for $P_{max} \approx 10$ mW. However in the output modeling of InGaAsP lasers where P may approach 60 mW, equation 1 is no longer valid. This is especially true for InGaAsP structures since P_S is typically 100 mW.

An expression for the gain reduction is derived that is valid for laser structures under large scale modulation

current. Successful modeling of device performance under large scale modulation can only be achieved by using the non-linear form of gain reduction derived in the next section. Only when confidence in the modeling technique is realized can the fundamental limits to DFB laser operation in an ultra-high speed communications system be pursued. Optical pulse parameters can be quantified with respect to spectral hole burning using system metrics of wavelength chirping and extinction ratio.

II. Intra-band Gain Saturation Theory

The derivation of the nonlinear gain for high power laser structures is outlined in this section. The expression for non-linear gain results in a diminishing optical gain as a function of increasing photon density in the active region. The intra-band relaxation time of the gain medium determines a critical power level for the device. If this critical power level is exceeded under modulation, large increases in rise and fall times are observed in the optical response. Excessive fall times may result in intersymbol interference (ISI).

The electric field in the laser cavity can be written as [1]

$$E(r,t)=\tfrac{1}{2}\hat{x}[\, E_0 U(r)\exp(-iw_0 t) + c.c.] \qquad (2)$$

in the single longitudinal mode [DFB] case where

w_0 -> optical frequency

$\hat{x}$ -> polarization vector

$U(r)$ -> spatial fundamental mode distribution in the cavity waveguide

Let $P(r,t)$ be the induced polarization expressed as

$$P(r,t)= \int_{w_g}^{\infty} \mu(w_T) D(w_T) (\sigma_{12} + \sigma_{21}) dw_T \qquad (3)$$

This equation is derived with the assumption of considering the response of a single two level system using the transition frequency w_T and summing all band to band transitions where

w_g -> band gap frequency

μ -> dipole moment

D -> joint density of states

σ_{12}, σ_{21} -> off diagonal density matrix elements

σ_{12} can be solved exactly for a two level system as [2]

$$\sigma_{12} = \frac{\mu \tau_{in}}{i\hbar} \frac{(\sigma_{11} - \sigma_{22})}{1 + i\delta} \frac{1 + \delta^2}{1 + \delta^2 + I} U E_0 \exp(-iw_0 t) \quad (4)$$

where

σ_{11} -> occupation probability for electrons in thermal equilibrium.

σ_{22} -> occupation probability for holes in thermal equilibrium

δ -> normalized detuning parameter

$$\delta = (w_T - w_0)\ \tau_{in} \quad (5)$$

I -> normalized intensity

$$I = \frac{| E_0 |^2}{I_S} \quad (6)$$

where

$$I_S = \{ (\mu/\hbar)^2 < | U(r) |^2 > \tau_{in}(\tau_c + \tau_v) \}^{-1} \quad (7)$$

and

τ_{in} -> polarization relaxation time

τ_c -> electron relaxation time

τ_v -> hole relaxation time

Note that (7) is an average intensity within the cavity and hence is not precise. However this assumption leads to a simpler analysis and implies an averaging over of the spatial holes burnt by the counter-propagating waves within the cavity. Carrier diffusion in semiconductor lasers does tend to "wash" the spatial holes, hence justifying the previous assumption [2]. The gain medium response to the applied field is determined by the susceptibility X.

Substitution of equ. (4) into (3) yields an induced polarization equation that can be expressed as

$$P(r,t) = (\epsilon_0/2) \left[XE_0U(r) \exp(-iw_0t) + c.c \right] \tag{8}$$

The susceptibility can be solved as

$$X = - \int_b^{\infty} \frac{1+ \delta^2}{1+ \delta^2 + I} \frac{f(\delta)\, d\delta}{\delta - i} \tag{9}$$

from this substitution where

$$f(\delta) = \frac{\Gamma \mu^2 D(\sigma_{11} - \sigma_{22})}{\epsilon_0 \hbar} \tag{10}$$

$$b = (w_g - w_0)\tau_{in} \tag{11}$$

where Γ is the modal confinement factor. This factor is introduced because $\sigma_{11} - \sigma_{22} = 0$ outside of the active region.

The susceptibility X is composed of real and imaginary parts.

$$X = X_R + iX_I \tag{12}$$

The susceptibility X can also be separated into linear and nonlinear parts where

$$X = X_L + X_{NL} \tag{13}$$

and

$$X_L = -\int_b^\infty \frac{f(\delta)d\delta}{\delta - i} \tag{14}$$

$$X_{NL} = I\int_b^\infty \frac{f(\delta)d\delta}{(\delta - i)(1 + \delta^2 + I)} \tag{15}$$

The evaluation of these integrals requires numerical methods [3]. However, an approximate analytic expression zfor the non-linear optical gain can be derived from the nonlinear susceptibility (14) using contour integration and the observation that the main integral contribution occurs when $|\delta| < 1$. Secondly, the induced susceptibility is related to the change in material dielectric constant, $\delta\epsilon$. $\delta\epsilon$ manifests itself as refractive index and optical gain deltas as seen in the relationship [1]

$$X = \delta\epsilon = 2n(\delta n - ig/2k_0) \tag{16}$$

where

n -> background index of refraction

k_0 -> propagation constant [w_0/c]

g -> optical gain

δn -> index change

It can be shown that

$$g_{NL} \approx - \frac{g_L I}{\sqrt{(1 + I)}\ (1 + \sqrt{(1 + I)})} \qquad (17)$$

The expression for nonlinear gain shows that the linear gain g_L is reduced by an amount of nonlinear gain g_{NL} as the optical intensity is increased. This effect is referred to as spectral hole burning. In semiconductor lasers the hole width ($\approx 10^{13}$/s) is almost identical to the spectral width of the gain profile because of the very short intraband relaxation time ($\tau_{in} \approx 0.1$ pS, as a result the linewidth = $\tau_{in}^{-1} = 10^{13}$/s). Therefore the gain medium saturates uniformly [1]. This implies that the given linear and nonlinear contributions to the optical gain are reduced similarly across a given frequency spectral range.

The total optical gain is

$$g = g_L + g_{NL} = \frac{g_L}{\sqrt{1 + I}} \qquad (18)$$

from (16) by re-arranging terms.

The linear gain in the gain medium can be expressed disregarding carrier diffusion effects as [2]

$$g_L = a(n - n_0) \qquad (19)$$

where

a -> differential gain coefficient

n -> carrier density

n_0 -> transparent carrier density

Equating a normalized photon density to I, coupled with (18) yields the following expression for optical gain as a function of n and S, photon density.

$$g(n,S) = \frac{a(n - n_0)}{\sqrt{1 + S/S_{sat}}} \tag{20}$$

where [4]

$$S_{sat} = \frac{\epsilon_0 n_m n_g \hbar}{\mu^2 w_0 \tau_{in}(\tau_c + \tau_v)} \tag{21}$$

and

n_m -> mode index of refraction

n_g -> group index of refraction

μ -> dipole moment

w_0 -> mode frequency

Notice that intra-band gain saturation does not occur for $\tau_{in} = 0$. For InGaAsP laser structures, τ_{in} is typically 100 fs. The conduction band relaxation time τ_c and the valence band relaxation time τ_v are 300 fs and 70 fs. These relaxation times are material dependent.

The saturation output power, P_{sat} is linearly related to S_{sat} through [4]

$$P_{sat} = \hbar_{out} \sigma_m v_g \hbar w_0 S_{sat} \tag{22}$$

where

η_{out} -> differential quantum efficiency of the output facet

σ_m -> optical mode cross-sectional area

v_g -> group velocity

The differential quantum efficiency and optical mode cross sectional area can be varied through DFB structure design. η_{out} may be varied, for example, by the coupling coefficient K which is a measure of the DFB grating coupling effectiveness of the forward and reverse propagating waves within the laser cavity. σ_m can be varied by changing the active region or stripe width. By decreasing η_{out} and σ_m, the saturation output power can be reduced for a particular DFB structure. As a result, a smaller fraction of intra-cavity photons are emitted from the laser [4].

Applying this observation to the denominator of the expression for optical gain (20) shows that a reduction or dampening of the optical gain occurs as the intra-cavity photon density is increased which is indicative of a poor efficiency laser structure. Using the newly defined optical gain term (20) it is time to proceed to the modeling of DFB InGaAsP laser structures with pre-determined saturation powers, P_{sat} under large scale, high speed modulation to study the carrier and photon densities' response.

III. Modeling of DFB Laser performance under high-speed, large signal modulation.

The nonlinear photon, carrier and phase rate equations can be expressed as follows [4],[5]

$$dS/dt = (\Gamma v_g g(n,S) - 1/\tau_p)S + R_{sp}(n) \quad (23)$$

$$dn/dt = I(t)/(qV) - n/\tau_n(n) - v_g g(n,S)S \quad (24)$$

$$d\Phi/dt = n_m/n_g(w - \Omega) + \tfrac{1}{2}\alpha(\Gamma v_g g(n,S) - 1/\tau_p) \quad (25)$$

where

- S -> photon density
- n -> carrier density
- Γ -> modal confinement factor
- v_g -> group velocity
- $g(n,S)$ -> optical gain as expressed in (20)
- τ_p -> photon lifetime
- $R_{sp}(n)$ -> spontaneous emission rate
- $I(t)$ -> applied current impulse
- q -> electron charge (Coul)
- V -> Active volume
- $\tau_n(n)$ -> carrier lifetime
- Ω -> longitudinal mode frequency at threshold value of mode index

The photon lifetime is expressed in the following form:

$$\tau_p = (v_g(\alpha + \alpha_{int}))^{-1} \quad (26)$$

where

α -> mode loss of the fundamental DFB mode (cm^{-1})

α_{int} -> internal cavity losses (cm^{-1})

The internal cavity losses α_{int}, are caused by free carrier absorption, heterostructure interface scattering and grating imperfections [5].

The carrier recombination rate $\tau_n(n)$ is modeled in its more accurate nonlinear form

$$\tau_n(n) = (A_{nr} + Bn + Cn^2) \quad (27)$$

where

A_{nr} -> non-radiative recombination rate due to trap and surface recombination

B -> Radiative recombination coefficient

C -> Auger recombination coefficient

The spontaneous emission rate $R_{sp}(n)$, was modeled as [5]

$$R_{sp} = \beta_{sp} B_{rad} n^2 V \quad (28)$$

where

$$\beta_{sp} = \frac{K\Gamma l^4}{4\pi^2 n_b n_m n_g V l_{sp}} \quad (29)$$

β_{sp} is referred to as the spontaneous emission factor and

K -> enhancement factor (1 for index guided structure)

l_{sp} -> spontaneous emission spectral width

n_b -> bulk material index

β_{sp} is between 10^{-4}- 10^{-5} for typical index guided InGaAsP structures.

The coupled rate equations were solved analytically using a Runge-Kutta approach [6]. The modeling software was written using RMB (Rocky Mountain Basic) and executed on a Hewlett Packard model 320 computer. The same software was also run using HTBasic on an AT&T 6386 Computer with math co-processor.

Initially, the drive current impulse was chosen to be a square wave with finite rise and fall times for two reasons. Agrawal used this response and hence colaboration of results could be achieved [4]. Secondly, most laser driver integrated circuits attempt to model this impulse. The square wave impulse was modeled using a super-gaussian function. The modulated signal could then be superimposed on a pre-bias current.

$$I(t) = I_b + I_p f(t) \tag{30}$$

where

$$f(t) = \exp\left[- \left[\frac{2|t|}{T_b} \right]^{\frac{Tb}{Tr}} \right] \tag{31}$$

where I_b -> pre-bias current (DC)

I_p -> peak modulation current

T_b -> bit duration (Bit rate -> B^{-1})

T_r -> rise/fall time

f(t) was bounded between 0 and 1.

The algorithm for determining DFB type laser dynamic response was developed as follows. Parametric data for the laser under investigation was entered. Two laser structures were considered. The first is designed to favor the energy gap mode as a consequence of an anti-reflective (AR) coated front facet and a highly reflective (HR) coated rear facet [7]. This structure is a folded-over version of a DFB laser with negligible facet reflectivity and a 1/2 phase shift at the center of the cavity. The output power is asymmetric with respect to the facets with the laser output predominantly confined to the front facet. Excellent mode selectivity is realized for this device.

The second structure is a 1/4 phase-shifted laser with low end facet reflectivities. The 1/4 phase-shifted device can be designed with intentions of realizing a somewhat uniform longitudinal mode intensity along the optical cavity. Locally intense regions of photon density coupled with the injected carrier distibution in the laser cavity causes spatial hole burning [8]. As a result, the carrier density varies throughout the active area which in turn causes a nonuniform refractive index. Hence the grating pitch is effectively changed throughout the medium which can vary the longitudinal mode intensity profiles.

DFB structure modeling techniques have been developed to assist device designers in minimizing spatial hole burning effects [9]. The magnitude of spatial hole burning is greater for the AR-HR structure mentioned previously. The large scale modulation current dynamic modeling presented here would more accurately portray a DFB structure with a uniform longitudinal modal intensity profile. Spatial hole burning can result in a nonlinear reduction of optical output power with increasing drive current. This spatial hole burning effect can sum with the spectral hole burning via intra-band gain saturation effect [9].

Typical values for the various device parameters are listed for a 1.55 μm DFB InGaAsP BH laser.

Variable	Description	Value	Units
a	differential gain coefficient	2.5×10^{-16}	
n_0	transparency carrier density	1.0×10^{18}	cm^{-3}
S_{sat}	saturation photon density	3.16×10^{16}	cm^{-3}
σ_m	optical mode cross section	1.0	μm^2
n_m	mode index of refraction	3.3	
n_g	group index of refraction	3.4	
μ	dipole moment	9.0×10^{-29}	cmC
w_0	free space mode frequency	1.21×10^{15}	s^{-1}
τ_{in}	intra-band relaxation time	100	fs

Variable	Description	Value	Units
τ_c	conduction band relaxation time	300	fs
τ_v	valence band relaxation time	70	fs
Γ	mode confinement factor	0.4	
v_g	group velocity	8.82×10^9	$cm \cdot s^{-1}$
act_w	active area width	2.0	μm
act_h	active area height	0.1	μm
act_l	active area length	250	μm
A_{nr}	non-radiative recombination rate	2×10^8	s^{-1}
B	radiative recombination rate	1×10^{-10}	$cm^3 s^{-1}$
C	Auger recombination coef.	3×10^{-29}	$cm^6 s^{-1}$
α	mode loss coefficient	25	cm^{-1}
α_{int}	internal loss coefficient	40	cm^{-1}

A modulation bit rate was chosen for the current drive pulse as well as a commom rise/fall time to be used in the super-gaussian expression in (31).

A peak modulation current was determined by multiplying the pre-bias current I_b by a factor. For large scale modulation the factor was chosen to be within the range 7-10.

The laser threshold current was calculated precisely in the following manner. A value for initial photon density,

S_{th} was assigned. Typically this value was in the order of 1-3 X 10^{12} $\cdot cm^{-3}$. The rate equation for carrier density (23) was set equal to 0 for the steady state condition. By iterating n, a solution was obtained for the carrier density at threshold , n_{th} using the rate equation (23) and the expression for optical gain (20) using minimization of delta n. Although the photon density at threshold is orders of magnitude below the saturation photon density this approach was used for accuracy. Also, if a pre-bias current above threshold was desired, it could be calculated accurately using this approach. The steady state current at threshold , I_{th}, was solved using equation (23)

$$I_{th} = (n_{th}/\tau_n(n_{th}) + v_g g(n,S_{th}) S_{th}) qV \qquad (32)$$

where

V -> Active area volume

I_{th} was usually assigned as the pre-bias current current I_b.

The Runge-Kutta technique was used to solve the coupled equations (23) and (24) throughout an interval consisting of a pre-determined number of bit increments. Usually 3 to 4 bit increments were necessary to solve for n and S until values approaching steady state were obtained. The number of temporal integration steps was variable. The usual value was 16000 across the 3-4 bit interval. The total

calculation time was 7 minutes using 16000 temporal steps on the Hewlett-Packard 320 computer.

The total facet output power was calculated from the photon density at each temporal increment using (22). Figures 1 and 2 show the facet power output and carrier density versus time for the DFB structure with parameters given previously at a modulation current frequency of 5 Ghz with 40 ps rise/fall times. The saturation power P_{sat} was chosen as 40 mW. The dotted trace on the figure is the modulation current waveform.

The frequency variation versus time was also calculated for the laser structure using the phase rate equation (25). As pointed out in the intra-band theory section, equation (16) shows that a change in carrier density determines an index of refraction change in the gain medium. This is also evident in the phase rate equation. Pulse amplitude modulation of a semiconductor laser inherently related to a change in carrier density via the coupled rate equations, results in a frequency or wavelength variation of the resultant optical pulse. The variation of the fundamental frequency is commonly referred to as frequency or wavelength chirp. The frequency chirp is derived in the following manner. The assumption is used that spectral hole burning results in a small depression in gain at the laser line. As

a result, an increase in carrier density is necessary to restore the gain.

If the gain is looked upon as a superposition of the dip due to spectral hole burning and the larger gain level in the absence of spectral hole burning, the Kramers-Kronig relation guarantees that the symmetrical dip in the gain which is the imaginary index will result in no net change in real index at the laser line. Therefore the only change is in the real index, which is the gain change in the absence of spectral hole burning [10]. This gain is g_L from (18). Using (17) and (18) yields an expression for g_L as a function of total gain g(n,S), and saturation power, S_{sat}.

$$g_L(n,S) = \frac{g(n,S)}{\left[1 - \frac{S/S_{sat}}{\sqrt{1+S/S_{sat}}\,(1+\sqrt{1+S/S_{sat}})}\right]} \tag{33}$$

The frequency chirp as a function of time can be expressed using (25) and the gain due to the real index in (33) as

$$\delta\nu(t) = \frac{\dot{\Phi}(t)}{2\pi} = \frac{\alpha}{2\pi}(\Gamma v_g g_L(n,S) - 1/\tau_p) \tag{34}$$

from (25) where the fundamental mode frequency Ω is assumed to coincide with Ω_0 at threshold. Therefore $\Omega - \Omega_0 = 0$ and at t=0, $\delta v(0)=0$ at the pre-bias threshold current. The linewidth enhancement factor is α.

The wavelength chirp, $\delta\lambda$ can be readily solved as [5]

$$\delta\lambda(t) = (-\lambda_0^2/c)\,\delta v(t) \tag{35}$$

Figure 3 shows the calculated wavelength variation, $\delta\lambda(t)$ versus time for the previously modeled device structure.

The linewidth enhancement factor is an important quantity in (34). This parameter is wavelength dependent. For 1.3 μm InGaAsP devices, the factor is 3-5. However at 1.55 μm, this factor increases to 10-15. The modeling of 1.55 μm device performance in this paper used an α of 10. The linewidth enhancement factor is defined as [11]

$$\alpha = \frac{dX_R(n)/dn}{dX_I(n)/dn} \tag{36}$$

where the separation of susceptibility into real and imaginary parts was shown in (12).

A further analysis of wavelength chirp characteristics of DFB lasers experiencing intra-band gain saturation was pursued. An actual measurement of wavelength chirping in the time domain is extremely difficult to achieve at modulation rates approaching 5-10 Ghz due to equipment limitations. A common technique invoked for chirp analysis is the time averaged wavelength spectrum technique. In this

procedure, the time averaged power intensity is recorded across the optical wavelength spectrum of interest using a conventional diffraction grating monochromator as the measuring instrument.

The delta wavelength modeling data of figure 3 in conjunction with the facet output power versus time data of figure 1 can be convolved to yield the time averaged optical power amplitude versus wavelength. For this analysis, the intra-cavity modal intensity was assumed to be constant. The 1/4 phase shifted device structure with low facet reflectivities could be used if it was properly designed. Spatial hole burning effects are therefore assumed to be uniform in nature.

The time averaged optical spectrum was computed as follows from the optical power and delta wavelength versus time data. First, a wavelength region of interest was chosen. Usually -/+ 4 nm around the fundamental wavelength was selected. The software was written to execute similarly to an optical spectrum analyzer using a periodic diffraction grating as it scanned across the wavelength range. The resolution of the analyzer was chosen to be 10 pm (10^{-12} m). The resolution bandwidth of the instrument was selected as 0.05 nm which is consistent with conventional 1/2-1 meter monochromators using diffraction gratings. Various filter shapes could be selected for measurement of the optical

power as the filter was swept across the wavelength range. One filter type employed equal weighting of all amplitudes within the resolution bandwidth. A second type used a parabolic shape with maximum weighting at the apex and -3 dB weighting at the edges of the band. The latter is more consistent with moveable diffraction type instruments.

As the "software" grating was swept across the region of interest, the discrete optical amplitudes corresponding to the temporal position of the delta wavelength vs. time data were summed appropriately by the selected resolution bandwidth filter. The time averaged power expressed in dB at the wavelength position l_m, was calculated using

$$P_{AVG}(l_m) = 10 \log_{10} \left[\frac{DC \sum_{i=1}^{N} P(l_i)W(l_i)}{T_b \sum_{i=1}^{N} 1/dt} \right] \qquad (37)$$

where

l_i -> discrete wavelength satisfying the filter as $l_m - \frac{1}{2}BW_{res} < l_i < l_m + \frac{1}{2}BW_{res}$

BW_{res} -> resolution bandwidth of the monochromator

$P(l_i)$ -> discrete power amplitude at l_i

$w(l_i)$ -> resolution bandwidth filter weighting function value at l_i

dt -> temporal increment of Runge-Kutta data array

DC -> duty cycle of modulation current

The DC value was usually in the range of 25 - 50 %.

Figure 4 shows the convolved time averaged spectra plot for the sample device with P_{sat}= 40 mW and B = 5 Ghz using 40 pS rise/fall times. The DC value was 33 %. Various parameters were computed from the raw spectral data. The short wavelength spectral width at - 30 dB was computed (SWL-W). This is the width of the spectrum calculated from the peak wavelength minus the short wavelength value that crosses the peak amplitude less 30 dB. A similar calculation was performed for the long wavelength side (LWL-W). The ratio in dB of the height of the observed cusp on the short wavelength side to the peak height (SWL-MHR) was also calculated.

The extinction ratio (ER) was also computed for each DFB structure under large scale modulation modeling. The ER is the ratio of optical power in the "OFF" state or bit slot to optical power in the "ON" state. The worst case ER was calculated using the power density throughout the bit slot as

$$ER = \frac{\langle P_{OFF} \rangle}{\langle P_{ON} \rangle} = \frac{\int_{t0+Tb}^{t0+2Tb} P(t)dt}{\int_{t0}^{t0+Tb} P(t)dt} \qquad (38)$$

where t0 was the temporal index from the modeled output power versus time response where the onset of the optical pulse due to the modulation current began. This onset was arbitrarily defined as 0.05 mW for the case of the pre-bias current I_b at laser threshold.

The derivation of wavelength chirp and ER were pursued in order to quantify the effects of intra-band gain saturation under large scale modulation on a DFB laser structure. These two parameters have major impact on the effectiveness of an optical source in an ultra-high speed pulse modulated lightwave communications system.

IV. Dynamic Modeling Results

Optical Output Power versus Time

Figure 5 shows the optical power output response vs. time for the modeled device structure as a function of saturation power, P_{sat} under large scale current modulation of $I_b + 10I_b$ at 5 Gbits using $0.2T_b$ or 40 pS rise/fall time. Note the underdamping of the relaxation oscillation for the device structure as P_{sat} is increased. A ringing pattern which is characteristic of an underdamped system is also evident for the 60 mW P_{sat}. The relaxation oscillation is due to an inherent resonance between the carrier and photon populations via stimulated emission. An approximate expression for the resonance frequency using small signal analysis is given by [5]:

$$\Omega_R = \left[\frac{1 + \Gamma v_g a n_0 \tau_p}{\tau_n \tau_p} \left(I/Ith - 1 \right) \right]^{\frac{1}{2}} \qquad (39)$$

where I is the drive current. For the given device structure used as an example thus far in this paper, the relaxation oscillation is approximately 11.7 Ghz using an I/Ith ratio of 10 for the large scale modulation current.

This ratio plays an important part in determining the relaxation oscillation frequency. The Ω_R is increased as a function of the drive current by the square root of I/Ith-1.

Note the increased optical fall time as a function of decreasing P_{sat}. This effect is examined more closely under the extinction ratio section.

Wavelength Chirping

The wavelength chirp is a significant factor in determining the performance of an ultra-high speed optical communications system. Laser linewidth broadening causes dispersion induced degradation over a long distance of fiber in some systems that may exceed 100 km. Dispersion penalties on the order of 5 dB can be realized from 1.55 μm DFB lasers at 2 Gbits through 120 km of fiber [12].

The magnitude of the relaxation oscillation via large delta n, determines the extent of wavelength chirping on the short wavelength side (SWL) of the spectrum. Figure 6 shows the calculated wavelength chirp for the device structure with different P_{sat} values at 5 Gbits. The current pulse rise time , T_r was $0.2T_b$ or 40 pS and a large scale modulation current using the super-gaussian expression was used. The SWL chirp is commonly referred to as time derivative or "transient" chirp [10]. The transient chirp

for a given device structure is directly proportional to the rise time of the modulation current impulse. Faster current pulse risetimes yield increased SWL chirp values. Figure 7 is a plot of the SWL chirp versus modulation current pulse rise time at 2 Gbit for the modeled device with a P_{sat} of 40 mW. The SWL chirp was analyzed in the large ($I_b + 10I_b$) and normal ($I_b + 3I_b$) scale modulation current cases where I_b was the device threshold current. The risetime was varied from 10 to 100 pS. Note the large SWL-W of 8.4 Angstroms (A) for the large scale modulation case at the fastest rise time of 10 pS. The normal modulation current exhibited 6 A SWL-W at 10 pS rise time. The SWL-W decreased linearly for both modulation current conditions, with the large scale type having a larger negative slope of 0.06 A/pS versus 0.02 A/pS.

Figure 8 shows the SWL-W for the modeled device with varying P_{sat} as a function of modulation rate from 1 to 10 GBits. The large scale current pulse risetime was fixed at $0.2T_b$. Observe that the 20 mW P_{sat} structure has almost negligible width across the frequency range. The calculated value was 0.2 Angstroms (A). This is due to complete gain saturation. As a result, the relaxation oscillation is completely suppressed, thereby eliminating the "transient" chirp.

The 40 and 60 mW P_{sat} SWL-Ws increase sublinearly with frequency under large scale modulation. The 60 mW P_{sat} structure exhibits higher SWL-W versus the 40 mW case due to less gain suppression; hence increased initial relaxation oscillation intensity upon turn-on. The maximum SWL-W was 11.6 A. It is interesting to note the collapse of the SWL-W for both structures. This is due to the nature of the optical pulse due to frequency response limitations of the structure, which consists of only the excitation of the initial relaxation oscillation at 8 and 9 Ghz for the 40 and 60 mW P_{sat} structures.

Figure 9 shows the long wavelength-width (LWL-W) for the modeled device under the same bias conditions as Figure 7. The LWL side of the measured optical spectra is called "adiabatic", which means that the quantity is frequency independent [10]. The LWL chirp results in a wavelength shift from the pre-bias value when the device transitions from the "ON" to "OFF" states. Note that the LWL-W is greater as a function of decreasing P_{sat} for the constant large scale modulation current case across the 1 to 10 Gbit rate band of interest. In fact, due to excessive intra-band gain saturation, the LWL-W for the P_{sat} of 20 mW case remains at 20 A throughout the frequency range. Notice the abrupt transition to larger LWL-W at 8-9 Gbit for the 40 and 60 mW P_{sat} devices, due to the optical output being confined

to the relaxation oscillation as pointed out in the SWL-W description.

From the chirp data modeled under large scale modulation, it was observed that net sum of the total wavelength deviation due to the real component of carrier induced index changes within the gain medium was a function of modulation frequency and was independent of saturation power except in the case of excessive gain saturation. Figure 10 shows the Total Spectral Width (TSW) as a function of modulation frequency using a rise time of $0.2T_b$. It is reasonable to assume that this is simply a conservation of energy between the dynamic carrier and photon populations. An underdamped structure (higher P_{sat}) will exhibit large SWL chirp, which results in a small LWL chirp. The inverse is also true. The ratio between the LWL and SWL chirps is governed by the degree of gain saturation.

The SWL and LWL chirp results using the nonlinear form of optical gain reduction in (20) are in good agreement with previous derivations of spectral hole burning gain reductions using a first order effect of a small degree expressed as [5],[10]

$$g(n,S) = g_L(n)(1-\epsilon S) \tag{40}$$

where $g_L(n)$ is the linear gain in (19) and ϵ is a constant that accounts for gain reduction. Using the derivation of frequency chirp in (33), the g(n,S) term which encompasses linear and nonlinear gain in this analysis is replaced by $g_L(n)$ in their analysis. Solving for $(\Gamma v_g g_L(n) - 1/\tau_p)$ in the photon density rate equation (23), substituting this result into (33) and adding the gain reduction term yields

$$\delta v(t) = \frac{\alpha}{4\pi} \left[\frac{1}{S} \frac{dS}{dt} - \frac{R_{sp}}{S} + \epsilon S \right] \tag{41}$$

This equation for frequency chirp shows the first term as the "transient" chirp because of the time dependence. The last two terms, consisting of spontaneous emission and gain reduction, correspond to the "adiabatic" portion of the chirp. The adiabatic terms cause the DC wavelength offset.

Figure 11 shows the peak or center wavelength (CWL) shift from the steady state value as a function of modulation frequency for the modeled device with varying P_{sat} values. P_{sat} for the saturated device is shifted almost 2 nm from the steady state value at threshold. As the degree of gain saturation is lessened, the CWL shift from steady-state also diminishes.

The wavelength chirp characteristics of modeled devices were also studied as a function of total optical output power. This analysis allowed viewing the device performance

via wavelength chirping through the onset of non-linear gain saturation due to spectral hole burning. The previously modeled device structure was used. The modulation rate was 5 Gbit using $0.2T_b$ or 40 pS current pulse rise time. P_{sat} was varied between 20 and 60 mW. The modulation current was ramped between I_b and $15I_b$. Figure 14 shows the SWL-W as a function of total optical power. It is interesting to note that the slope of the SWL-W varies considerably across the P_{sat} values. The high P_{sat} structure (60 mW) exhibits SWL-W that increases sublinearly due to the onset of gain reduction. The slope remains fairly constant for the 40 mW P_{sat} case. The slope is negative for the 30 mW case due to excessive hole burning that reduces the relaxation oscillation amplitude con-siderably across the total power output region of interest.

The LWL-W increased linearly for all structures as the total power output increased. As expected, due to large adiabatic chirp, the 20 mW P_{sat} structure showed the largest LWL-W.

The peak or center wavelength shift versus the steady state value yielded interesting results in this analysis as shown in figure 15. The peak wavelength shift was increasingly negative (blue shift) as the gain saturation worsened. As shown earlier, this is due to spectral hole burning via intra-band gain saturation. However, the peak

wavelength shifts to longer wavelengths (red shift) with low modulation currents of $2I_b$ to $4I_b$. For high saturation power structures, at low modulation currents using a 5 Gbit current pulse, the optical response consists solely of the initial relaxation oscillation. The optical power output resides in the region of the large carrier density swing due to the relaxation oscillation. Crossing from the time to frequency domain implies that the peak wavelength shift is blue referenced to the the steady state value.

As the modulation current increases slightly, the more familiar underdamped optical pulse response is generated as in figure 1. The resultant peak optical power in the wavelength regime is transferred due to a subsequent carrier density oscillation to a longer or more red wavelength yet still blue compared to the the steady state value. Further increase of the modulation current then introduces the nonlinear gain reduction effects that accounts for the increasing blue shift of the peak wavelength (adiabatic chirp).

Characteristics of the fine structure of the modeled wavelength spectrum also should be noted. Many device structures exhibited asymetrical cusps or peak regions on both sides of the peak wavelength. By observing the delta wavelength and carrier density versus time plots it was apparent that these are due to regions of short temporal

duration where the carrier density varies slowly. Therefore minor peaks are formed in the optical intensity versus optical wavelength domain. The minor peak on the short wavelength side corresponds to the carrier density swing through the initial relaxation oscillation. The peak(s) on the long wavelength side are the result of subsequent carrier population relaxation and/or the carrier level shift upon the "ON" to "OFF" transition.

From a systems perspective, a device structure with low total spectral width under modulation is desirable. A smaller total spectral width was realized as the saturation power was decreased, providing that the structure was not operated under excessive gain saturation. This is due to the suppression of the "transient" chirp. The modulation frequency also impacts the total spectral width (TSW). Subsequent relaxation oscillations may be suppressed with increasing modulation frequency which alters the optical pulse shape dramatically. The wavelength chirp characteristics are then shifted as shown in figures 8 and 9.

Gain reduction can be accomplished by decreasing the photon lifetime within the cavity by reducing the differential quantum efficiency, η_{out}, or reducing the optical mode cross-sectional area σ_m as seen in the expression for P_{sat} (22).

Extinction Ratio (ER)

The modeled results for the super-gaussian large scale modulation current yield interesting results for ER. Figure 12 shows the ER versus frequency for the sample device modeled with differing saturation powers. The modulation current was $10I_b$ and the risetime was $0.1T_b$. Note the extremely poor ER for the device with the lowest saturation power of 20 mW. In Figure 5, observe the long fall time of the P_{sat}= 20 mW structure. In fact, the optical tail extends into the next two bit slots. The fall time appears to be independent of modulation frequency. Therefore as the modulation frequency increases, the portion of optical power in the adjacent bit slot increases due to the fall time tail extension. This observation accounts for the fairly linear dependence of ER versus modulation frequency as shown in Figure 12.

When the modulation current risetime is increased to $0.2T_b$, as shown in Figure 13, the ER improves for all saturation power cases. The ER decreased 10 % from 0.25 to 0.225 for P_{sat}= 20 mW. Note the nonlinearity of ER versus frequency for frequencies less than 3 Ghz.

Under large scale modulation of $10I_b$, the high ER is unacceptable for the 20 mW saturation power structure. The

system penalty would be too severe since an ER of 0.25 allows only 6 dB of margin.

The maximum operating device output power was evaluated for the 20, 40 and 60 mW P_{sat} devices at 5 Gbits in order to maintain a minimum of 0.025 or 16 dB ER. The peak modulation current was ramped between $3I_b$ and $15I_b$ and the rise time was preserved at $0.2T_b$. The time averaged optical power in the "ON" bit, P_{ON}, was found by summing the discrete optical power values in the "ON" bit slot of duration T_b and dividing by the number of summed power points. It was found that if $P_{ON} < P_{sat}/4$ then the 0.02 ER could be maintained at 5 Gbits for all P_{sat} values slightly above 20 mW. This quantifies a limit for the maximum optical power to be realized from a DFB semiconductor laser for high speed systems applications, by taking into account only the effects of spectral hole burning due to intra-band gain saturation. Also, since the optical fall time appears independent of the modulation frequency under intra-band gain saturation, as the frequency increases above 5 Ghz, the ER will worsen using the $P_{sat}/4$ ratio.

Increasing intra-band gain saturation through a lowering of P_{sat} limits the maximum optical power of DFB laser structures under large scale modulation insofar as maintaining a low ER for the high speed communications system. P_{sat} can be increased by lessening the spectral

hole burning effects through increased differential quantum efficiency η_{out}, and increasing the modal cross-sectional area σ_m from (22). This contradicts the desired increase in intra-band gain saturation prescribed to decrease the SWL chirping. By using a conventional square wave modulation current with finite rise and fall times in (31), the maximum power of the laser at a particular P_{sat} is fundamentally limited to a significant level below the saturation power for system use.

V. Optimization of Laser Optical Output Response using Modulation Current Shaping

The super-gaussian square wave format for the laser modulation current can be improved upon in order to realize an optimum optical pulse with minimization of total wavelength chirp and ER when the device is operated below the structure saturation power, P_{sat}.

Referring to (41), the transient portion of the frequency chirp is governed by the rate of photon density change. If the dP/dt can be suppressed, a corresponding decrease in the short wavelength chirping can be realized. This can be accomplished by suppressing the amplitude of the initial relaxation oscillation during turn-on. Through proper modulation current pulse shaping, it can be be shown that the transient chirp can be nearly eliminated, resulting in a nearly gaussian optical pulse shape under large scale modulation current.

The concept of current pulse shaping to minimize laser dynamic spectral width was reported by Olshansky and Fye [12]. Their approach neglected the effects of gain saturation and hence is applicable to laser operation well below the onset of intra-band gain saturation due to spectral hole-burning. The modeling technique used in [12]

also assumed a fixed superposition of an initial current impulse with the main current pulse.

The approach taken in this study was to strive for a minimization of carrier density fluctuation in order to assure the reduction of transient chirping due to relaxation oscillations upon turn-on. The previously defined photon and carrier density rate equations (23),(24) were satisfied in their entirety using the nonlinear form of gain in (20). No predetermined attributes of the modulation current were assigned. Through multiple iterations of the rate equations, the necessary modulation current was calculated at each temporal increment in order to satisfy boundary conditions for the carrier density.

The modeling for the modulation current pulse shaping was performed in the following manner. First, the device characteristics were chosen, including modulation bit rate, and pulse rise and fall times. A reference response was calculated using the Runge-Kutta method detailed earlier in order to acquire initial power, carrier and wavelength chirping data using the super-gaussian form of the modulation current. A target carrier density was then selected. This value was chosen with a desired peak optical power output in mind.

The allowable variation in carrier density was then selected. Typically the maximum deviation of 0.05% was

chosen. Since the drive current was varied to obtain the target carrier density, a step size was chosen on the basis of the allowable deviation in carrier density. Usually a step size of 0.1 milliamperes was selected.

Further constraints were also placed on the current. A maximum value was selected for dI/dt in order not to exceed a realistic value for each portion of the solution.

The intent of the modeling was three-fold. First, vary the carrier density as rapidly as possible from the pre-bias value to the desired carrier density at optical turn-on. Secondly, keep the carrier density constant until such time that the optical pulse duration will be consistent with the allowable bit period, taking into account the allowable rise/fall times of the modulation current. Lastly, decrease the carrier density until the pre-bias state is obtained once again. The 'trick' in the technique is to suppress the initial relaxation oscillation in order to minimize the transient chirp. The DC chirp value which is dominated by the carrier density transition from ON to OFF state will always be present and the extent varied only by the target carrier density.

Initially, the current was shaped as a super-gaussian using the selected rise/fall time. The rate equations were repeatedly solved as a function of increasing current pulse amplitude until the target carrier density was achieved to

within the selected deviation. At this point, the initial relaxation oscillation as manifested through the carrier density, has been acquired for the device structure. The drive current is then resumed from where this initial impulse meets the bias current minimum (pre-bias) as mandated by the maximum dI/dt. From this temporal point and beyond, the modulation current I, is iterated using the value of current from the previous temporal point as the starting value. The current value could be iterated positively, negatively or even remain the same as the carrier density requirements for the particular desired solution were being satisfied.

The rate equations are continually updating the carrier and photon densities through the previously described Runge-Kutta technique using the newly defined modulation current waveform. This process is continued until the carrier density has been at the ON level for the necessary time duration to satisfy the bit timing requirements. After the bit timing is satisfied, the newly constructed modulation current is allowed to return to the pre-bias level within the dI/dt constraints.

Figure 16a is a comparison of the super-gaussian (NORMAL) versus the shaped modulation current impulse in the large signal regime. The optical power output plots are shown. The device structure was modeled using a P_{sat} of 60

mW. The normal pulse shape was contructed at 5 Gbit with 40 pS rise/fall times. The target carrier density was selected as 1.79 X 10^{18} cm^{-3} for the following reason. In order to make a fair comparison between the response of the laser structure to the normal and shaped current waveforms, the resultant total optical power should be equivalent. Referring to the P(Power) versus time plot for the shaped current case, note the nearly gaussian shape of the resultant power output pulse. The initial relaxation oscillation has been entirely dampened compared to the normal optical output power response. The carrier density versus time plots are shown in figure 17. Notice that the shaped carrier density shows little deviation from the desired clamping point of 1.79 X 10^{18} cm^3 in figure 17a.

Figures 18 and 19 compare the normal and shaped modulation current with respect to wavelength chirp and actual drive current waveform. The derived current for the shaped response , figure 19a, exhibits a minor pre-pulse , followed by the large amplitude significant duration major pulse. The pre-pulse is the current versus time required to excite the relaxation oscillation to the desired carrier density level. The major current pulse then follows after a duration approximately equal to the inverse of the relaxation oscillation frequency. From the expression for the relaxation oscillation frequency (39), in this case at a

modulation current of $10I_b$, the approximately 12 Ghz relaxation frequency results in an 85 pS time lapse between the pre-pulse and the major pulse. The pre-pulse then produces and sustains the initial relaxation oscillation until the main current component is required to maintain the carrier density at its desired value.

Figure 18a shows a large reduction in total wavelength chirp for this device structure. In fact, compared to the super-gaussian modulation current waveform, the short wavelength width has been reduced by a factor of 45 from 9.4 to 0.2 A. The long wavelength width has increased by 40% from 7.2 to 10.4 A. The LWL shoulder is reduced by 3 dB however, from -13 to -16 dB from the peak wavelength amplitude for the shaped case. The increased adiabatic chirp for the shaped current results from the larger delta n encountered from pulse ON to OFF state due to the clamping of the carrier density at a higher level than that obtained at turn-off using the super-gaussian modulation current (figure 17a). The peak wavelength has also shifted 3 A more blue for the shaped response (1549.26 compared to 1549.54) from the steady-state value of 1550 nm which is indicative of the larger carrier density swing at turn-off.

The TSW has decreased significantly for the shaped case, by 36 %, from 16.6 to 10.6 A. The reduction of TSW at

-10 dB from the peak wavelength amplitude is a factor of 10 from 2 to 0.2 A for the shaped case.

Figure 20b shows modeled data for the device structure with a P_{sat} of 60 mW and 5 Gbit modulation rate, comparing total spectral width due to chirping as a function of total optical power for the normal and shaped current impulses. The pulse rise/fall times were chosen as $0.2T_b$ for the normal case. Significant reduction of chirp can be realized across a broad range of optical output power, even through the onset of intra-band gain saturation as shown in the figure. From figure 20a, it is evident that the ER has decreased by a factor of 2 from the super-gaussian to shaped current impulses. The ER and total wavelength chirp in figure 20a and 20b were plotted as a function of time averaged power in the ON bit slot in order to make a reasonable comparison between the methods to account for the onset of gain saturation effects.

Current pulse shaping can be very beneficial in optimizing DFB laser performance under large scale modulation in an ultra-high speed communications system. The large reduction in ER allows for increased receiver dynamic range. The significant decrease in wavelength chirp will lessen the fiber dispersion effects on the launched optical pulse, possibly allowing for increased repeater

spacing compared to a conventional square wave type of current modulation.

Tailoring of the current pulse could be accomplished through mixing of the pre-pulse with the phase shifted major pulse in order to arrive at a waveform approximating the theoretically derived impulse. A microwave driver circuit with a resonance at the laser relaxation frequency could possibly be adapted to yield the desired waveform. One large drawback to a shaped current impulse is the need to customize the waveform for optimum response, i.e. proper amplitude of pre-pulse and temporal phase shift between the pre and major pulses. These attributes of the modulation current are dependent upon the device saturation power and relaxation oscillation frequency which may differ broadly across a population of processed devices from a single wafer. For example, in DFB structures as discussed in this paper, the differential quantum efficiency of the output facet of interest, η_{out}, and total efficiency may differ by more than 20% at a constant KL due to the random phase shifts encountered by the intra-cavity propagating waves from the last complete grating corrugation to the respective front or rear facet [5].

In order to optimize dynamic performance with respect to minimization of wavelength chirp, the design of the current modulator circuit should be robust enough to provide

"tuning" to compensate for varying degrees of gain reduction and relaxation oscillation frequencies.

VI. Onset of Gain Saturation: Experimental Results

The time averaged optical spectrum and time domain pulse responses were studied for 1.55 μm BH DFB laser diodes with asymmetric facet reflectivities in order to verify modeled gain saturation due to spectral hole-burning effects. Spatial hole burning effects were inevitable for these devices due to the HR-AR facet coatings. Spatial hole burning effects however have the same effect as spectral hole burning on device performance; i.e..increased gain saturation. The linewidth enhancement factor α, was assumed to be similar between the devices.

The onset of gain saturation was observed through features of the wavelength chirping and optical response in the time domain. The modulation rate was chosen as 5 Gbits. The test set up is shown in figure 21. The devices were tested in chip form. The pre-bias current was supplied to the device at the calculated threshold current from a previous L-I-V scan. The test temperature was 20 degrees C. The modulation current was a 50% duty cycle square wave from a high power pulse generator. The frequency source for the generator was provided by an external clock. The rise and fall times of the modulation current could also be varied by the amplitude of the clock signal.

The devices were tested at two modulation currents which were 40 mA and 96 mA, that are typical of normal ($3I_b$) and large ($7I_b$) scale modulation given the threshold current (I_b) of 14 mA for the two devices shown. The 96 mA was the largest value obtainable with the pulse generator. The modulation current waveform at 40 mA is shown in figure 22. Note that the risetime at 5 Gbit was 44 pS and the fall time was 38 pS.

The optical output of the laser under test was coupled to a micro-lensed single mode fiber and then through an optical isolator to the measurement apparatus. The output could be connected to an ultra-high speed photodetector with a 3 dB optical bandwidth of 20 Ghz which was then terminated to a high speed sampling oscilloscope. The coupled light output could also be routed to an optical spectrum analyzer (OSA) for the time averaged spectrum measurement. The OSA used in this study had a resolution bandwidth of 0.7 A at 1550 nm.

Figure 23 shows the optical pulse and time averaged spectral responses for two devices under test (DUT) at 5 Gbit using the "normal" scale modulation current of 40 mA. DUT 1 has an estimated P_{sat} of 15 mW versus a P_{sat} of 25 mW for DUT 2 at 20 deg C. The calculated SWL-W is 0.73 nm for DUT 1 with the lower saturation power, compared to 0.79 for DUT 2. The smaller transient chirp for DUT 1 is due to the

smaller relaxation oscillation power amplitude above the subsequent oscillation that also results in a reduction of dP/dt for DUT 1 as shown in (41). The dP/dt for the initial relaxation oscillation, using the photodetector responsivity in volts from the oscilloscope display (figure 23) is 0.8 mV/pS for DUT 1 and 1.1 mV/pS for DUT 2.

Note the cusp or minor peak on the SWL side of the optical spectra for both devices. This agrees quite well with the modeled time averaged spectrum results. As shown in the modeling section, this local maximum corresponds to the peak excursion of the carrier density during the initial relaxation oscillation. Since the carrier density is varying slowly with time in this region of largest delta n from the average carrier density state, the time averaged power amplitude in the frequency (wavelength) domain will be larger hence resulting in a minor peak in the spectral response.

The spectral resolving capabilities of the OSA due to stray light levels may assist in giving the appearance of a finite slope from the minor peak to the background or low-level spectra response of the device which is due to Fabry-Perot and spontaneous emission effects.

The adiabatic chirp (LWL-W) is larger for DUT 1 (0.45 versus 0.34 nm) indicative of a larger carrier density swing from the ON to OFF state at 40 mA modulation current

for this laser. This is consistent with the modeling results.

Figure 24 shows the time resolved optical and time averaged spectral results for DUT 1 and 2 using the large scale modulation current of 96 mA at 5 Gbit. Both devices exhibit significant dampening of the inital relaxation oscillation upon turn on compared to the next oscillation. Note the second oscillation in the optical responses which is due to a subsequent carrier oscillation which is not heavily dampened for both structures. Therefore, even DUT 1 with lower saturation power is not in excessive gain saturation using 96 mA modulation current at 5 Gbit. From the DC (Direct Current) L-I-V curves, DUT 1 and DUT 2 were operating at 70% and 50% of the maximum light rollover power. However, the initial relaxation oscillation of DUT 2 is less suppressed than that of DUT 1, due to lower gain saturation for DUT 2, which is evident by the larger dP/dt of the initial oscillation and larger overshoot of the oscillation.

As a result of the under damped responses, minor peaks on both the SWL and LWL sides of the peak wavelength spectrum are observed, which is consistent with the theoretical results shown earlier. The minor peaks have maximum amplitudes that are proportional to the deviation of the optical response from an average optical power value

P_{avg} in the ON state. This follows from the dn/dt to dS/dt proportionality assuming gain saturation effects are comparable yet not identical for the devices evaluated here.

DUT 2, which has a 60% higher Psat value than DUT 1, exhibits asymmetric peaks in the optical spectra data, where the amplitude of the SWL peak is 7 dB less than the LWL peak. The SWL-W is 1.03 nm which is also significantly wider than the value of 0.72 nm for device 1.

DUT 2 has shown a 30 % increase in SWL-W from 0.79 to 1.03 nm as the modulation current increased. This is consistent with modeling data shown in figure 14 which shows the SWL-W as a function of time averaged power. For a device with relatively high P_{sat}, (DUT 1), the SWL-W increases sublinearly with increasing modulation current as long as the output power is below the saturation level.

DUT 1 on the other hand, exhibits the same SWL-W with increasing modulation current. This is indicative of a device with lower P_{sat} from figure 14 (< 30 mW). The offset in P_{sat} values from the modeling to experimental case may be due to modeling parameters, including an optimum output power level of 100 mW which may be too high than the actual value for DUT 1 and DUT 2. Secondly, the determination of P_{sat} was based on DC versus pulsed L-I-V measurements which could give lower values due to thermal effects. Thirdly,

spatial hole burning effects will sum with the spectral hole burning gain reduction effect.

The time resolved optical response is indicative of the carrier transitions and consequently can be evaluated to shed light on the frequency domain response. The initial relaxation oscillation traverses farther from the P_{avg} point in the ON state and varies more quickly at the peak excursion of the initial relaxation oscillation than at the basin below the P_{avg} point before the next oscillation begins. As a result, the convolution would yield asymmetric peaks in the wavelength domain, with the SWL minor peak amplitude less than the LWL minor peak. This reflects the measured optical spectrum for the device.

In figure 24, the optical response of DUT 1 exhibits a more heavily dampened initial relaxation oscillation compared to DUT 2 due to increased gain saturation. Observe that the initial relaxation deviates 8 mV from the P_{avg} value of the waveform which is nearly equivalent to the extent of the basin below P_{avg} before the subsequent oscillation. As a result, the frequency domain exhibits symmetry between the spacing of the SWL and LWL minor peaks which have nearly equivalent amplitudes.

Both devices exhibited fall times of nearly 90 pS at 5 Gbits with 40 mA modulation current which would result in poor ER of 0.05. Under large scale modulation current of 96

mA, the fall times increased to over 100 pS for both devices with an estimated ER of 0.15 for both devices.

The adiabatic chirp increased by 35 % from 0.45 to 0.62 nm for the lower P_{sat} DUT 1 upon the transition from 40 to 96 mA modulation current. DUT 2 showed a similar increase from 0.39 to 0.55 nm.

VII. Conclusion

Lightwave system parameters including ER and wavelength chirping were modeled for a DFB semiconductor laser using the phase, photon and carrier density rate equations. The convolution of the optical power response with the index of refraction variation in the active region related to the linear carrier density change yielded the time averaged wavelength response. The large scale modulation current regime was explored in detail at ultra-high bit rates exceeding 5 Gbits using the derived nonlinear gain expression that includes spectral hole burning effects.

The ER for a device could be improved upon under large scale modulation by increasing the differential quantum efficiency, η_{out}, and the modal cross-sectional area, σ_m. However, transient wavelength chirp increases with larger saturation power, P_{sat}. This increased linewidth can result in unwanted fiber dispersion effects in a high speed communications system. Consequently, a compromise must be used to balance the net effect of the two terms using conventional modulation techniques.

Optimization of the optical pulse response was achieved at 5 Gbit through shaping of the modulation current impulse. By clamping the carrier density at a pre-determined level,

the initial relaxation oscillation was completely suppressed. Therefore the transient portion of the wavelength chirp was eliminated. The adiabatic or long wavelength portion of the chirp increased slightly due to a higher carrier density at pulse turn-off compared to modeling using the super-gaussian current impulse.

Through pulse shaping, the ER and total wavelength spectral width decreased by 60% and 36%, under large scale modulation for a typical device structure with a saturation power of 60 mW. Most impressive was the factor of 10 reduction in spectral linewidth from 2 to 0.2 A at the -10 dB level from the peak spectral amplitude. It appears possible to construct such a pulse shaping circuit that would supply the minor pre-pulse current required to excite the initial relaxation oscillation, before the large injected current is necessary is to sustain the optical output. Such a circuit could optimize the laser optical performance in a high speed communications system.

The optical pulse response and time averaged optical spectra were measured for devices at 5 Gbits at normal and large scale modulation current levels to observe the onset of gain saturation due to spectral hole burning. Spatial hole burning effects were not taken into account. However the net result is lower optical gain for the fundamental mode with increased modulation current. Increased adiabatic

chirp was observed for the devices as the modulation current increased. The device with lower P_{sat} exhibited the same SWL-W under normal and large scale modulation which is consistent with a device with a P_{sat} between 30 to 40 mW from the modeling data of figure 14. The device with larger P_{sat} showed a 30 % increase in SWL-W from 0.79 to 1.03 nm from normal to large scale modulation current. This agrees with the over 40 mW P_{sat} data from figure 14 which shows a sublinear increase of SWL-W with increased optical power output.

Lastly, the laser dynamic modeling developed herein could be enhanced to portray DFB devices more realistically. Axial variations of the optical mode intensity and specifically spatial hole burning can cause perturbations in the effective DFB grating in the structure causing shifting of the peak wavelength within a modulation cycle. The transfer of large optical gain to other supported waveguide modes may also occur. Leakage currents and carrier diffusion could also be accounted for in the modeling.

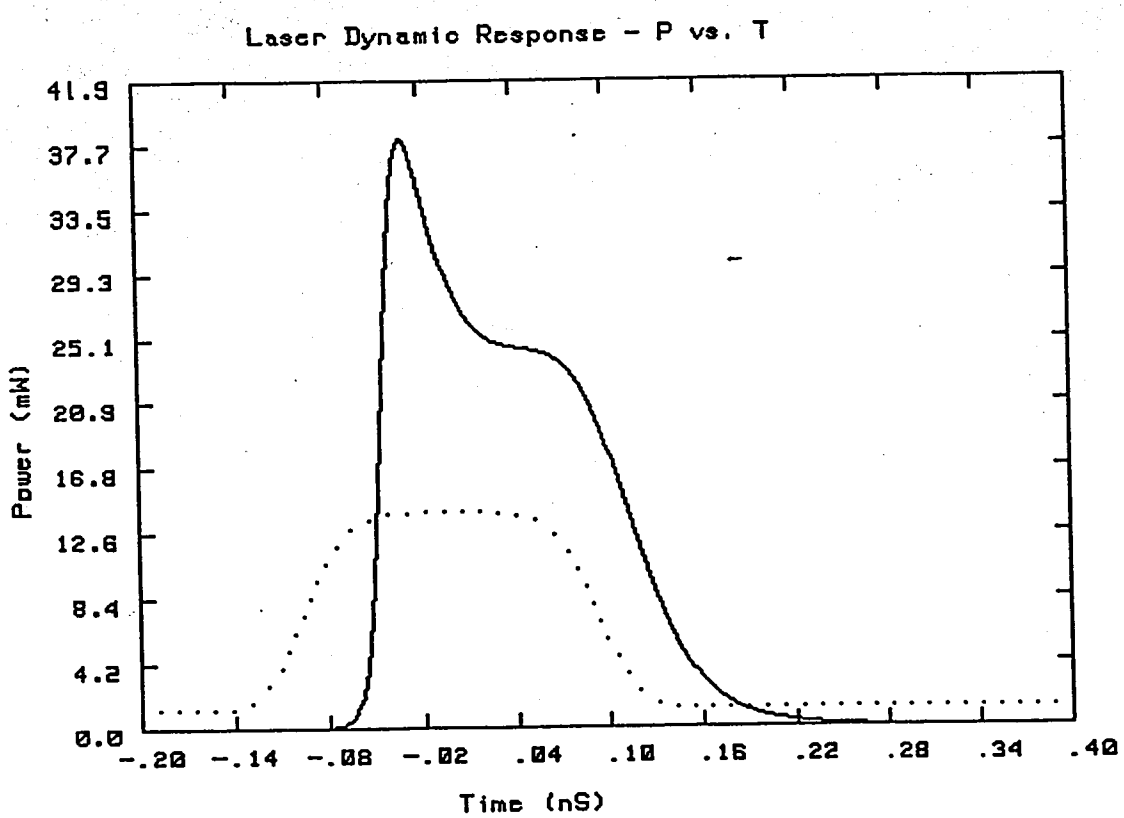

Ith= 11.854 mA
Sth= 2.00000E+12 /cm3
Ssat= 2.87639E+16 /cm3
Psat= 40.000 mW
P(Ith)= .0028 mW
Tau_p= 1.745 pS
Alpha_bar= 25.0 cm-1
Alpha_int= 40.0 cm-1
Kappa= 50.0 cm-1
N(Out)= .123

Nth= 1.65008E+18 /cm3
Tau_n(Threshold)= 2.239 nS

Ipeak= Ith+10.0*Imod
Ipeak= 118.539 mA
Mod Frequency= 5.0 Ghz
Rise/Fall Time= 40.0 pS
Linewidth EF= 10.0

Integration Step= 1500.00 fS

Figure 1. Facet output power versus time (Super-gaussian pulse, 40 mW P_{sat}, 5 Gbit)

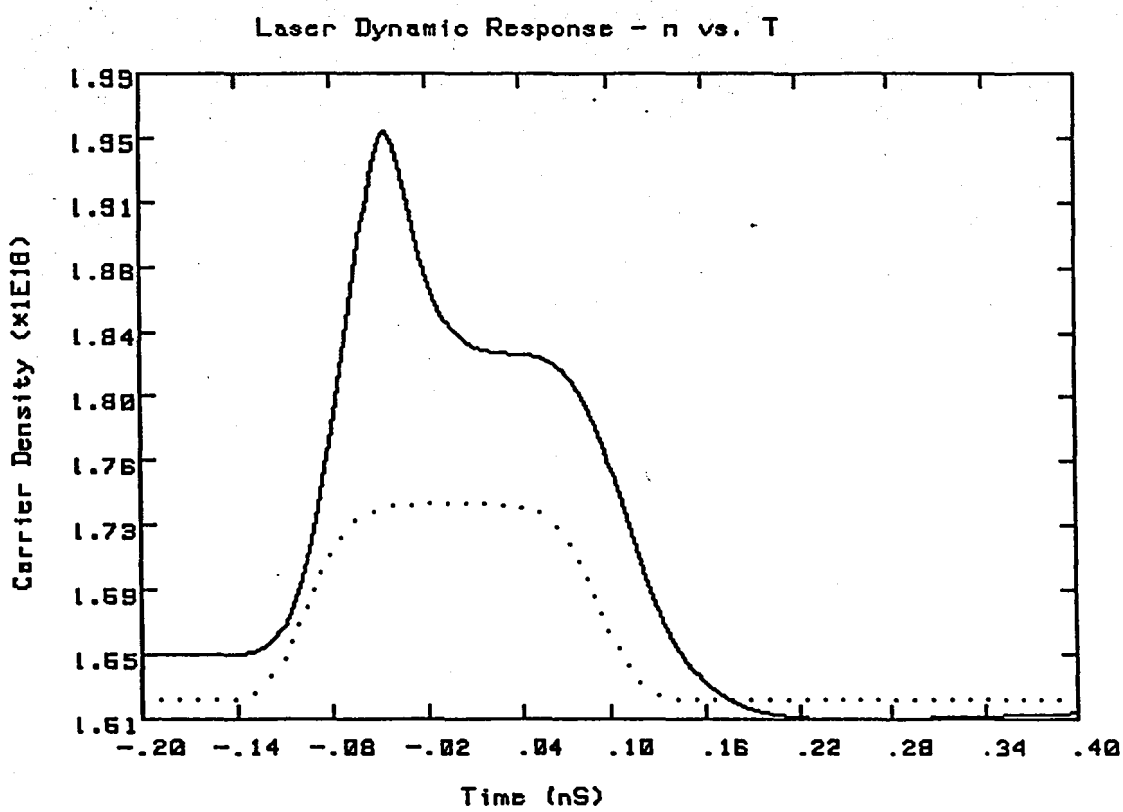

Ith= 11.854 mA
Sth= 2.00000E+12 /cm3
Ssat= 2.87639E+16 /cm3
Psat= 40.000 mW
P(Ith)= .0028 mW
Tau_p= 1.745 pS
Alpha_bar= 25.0 cm-1
Alpha_int= 40.0 cm-1
Kappa= 50.0 cm-1
N(Out)= .123

Nth= 1.65008E+18 /cm3
Tau_n(Threshold)= 2.239 nS

Ipeak= Ith+10.0*Imod
Ipeak= 118.539 mA
Mod Frequency= 5.0 Ghz
Rise/Fall Time= 40.0 pS
Linewidth EF= 10.0

Integration Step= 1500.00 fS

Figure 2. Carrier density versus time (Super-gaussian pulse, 40 mW P_{sat}, 5 Gbit)

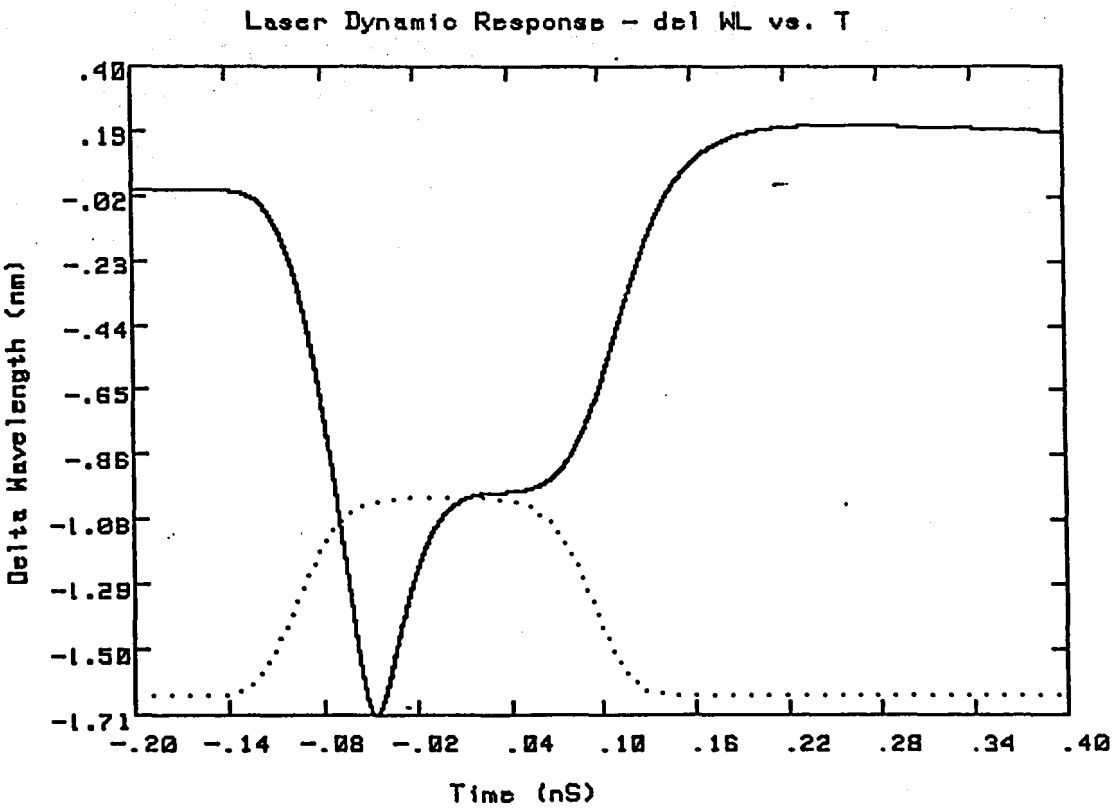

Ith= 11.854 mA
Sth= 2.00000E+12 /cm3
Ssat= 2.87639E+16 /cm3
Psat= 40.000 mW
P(Ith)= .0028 mW
Tau_p= 1.745 pS
Alpha_bar= 25.0 cm-1
Alpha_int= 40.0 cm-1
Kappa= 50.0 cm-1
N(Out)= .123

Nth= 1.65008E+18 /cm3
Tau_n(Threshold)= 2.239 nS

Ipeak= Ith+10.0*Imod
Ipeak= 118.539 mA
Mod Frequency= 5.0 Ghz
Rise/Fall Time= 40.0 pS
Linewidth EF= 10.0

Figure 3. Delta wavelength versus time (Super-gaussian pulse, 40 mW P_{sat}, 5 Gbit

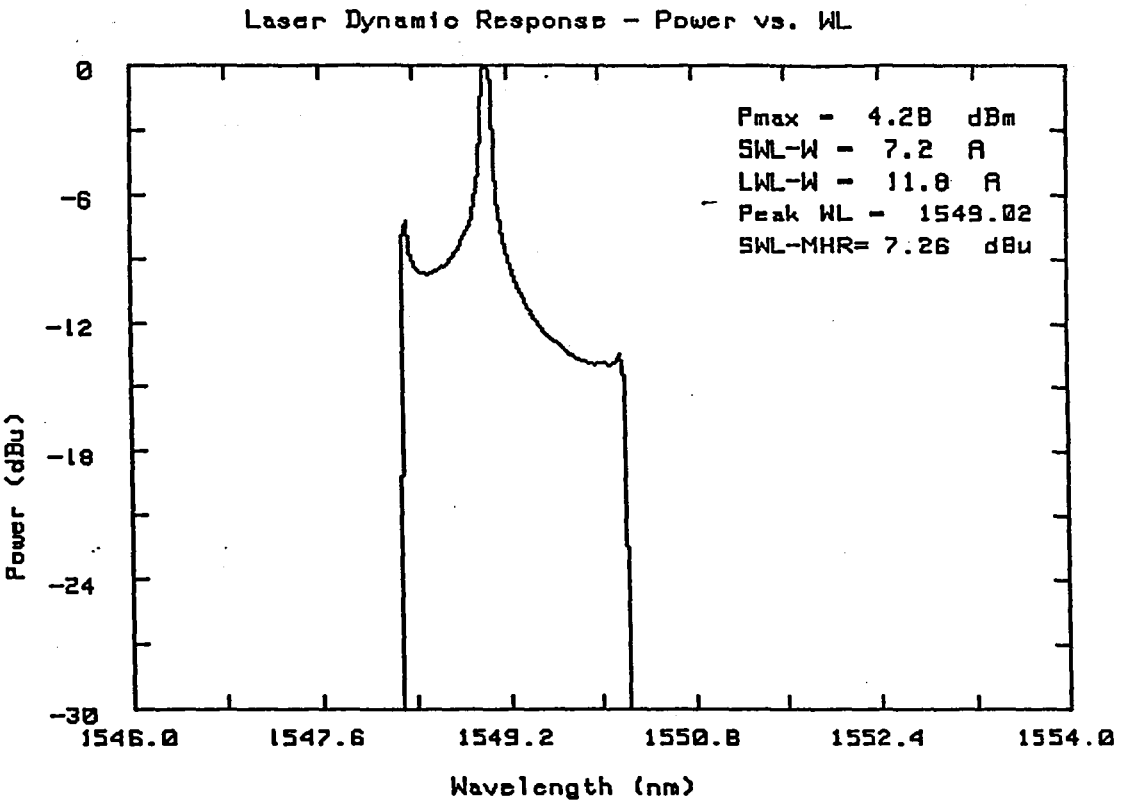

Ith= 11.854 mA
Sth= 2.00000E+12 /cm3
Ssat= 2.87639E+16 /cm3
Psat= 40.000 mW
P(Ith)= .0028 mW
Tau_p= 1.745 pS
Alpha_bar= 25.0 cm-1
Alpha_int= 40.0 cm-1
Kappa= 50.0 cm-1
N(Out)= .123

Nth= 1.65008E+18 /cm3
Tau_n(Threshold)= 2.239 nS

Ipeak= Ith+10.0*Imod
Ipeak= 118.539 mA
Mod Frequency= 5.0 Ghz
Rise/Fall Time= 40.0 pS
Linewidth EF= 10.0

Figure 4. Optical Intensity versus wavelength (Super gaussian pulse, 40 mW P_{sat}, 5 Gbit)

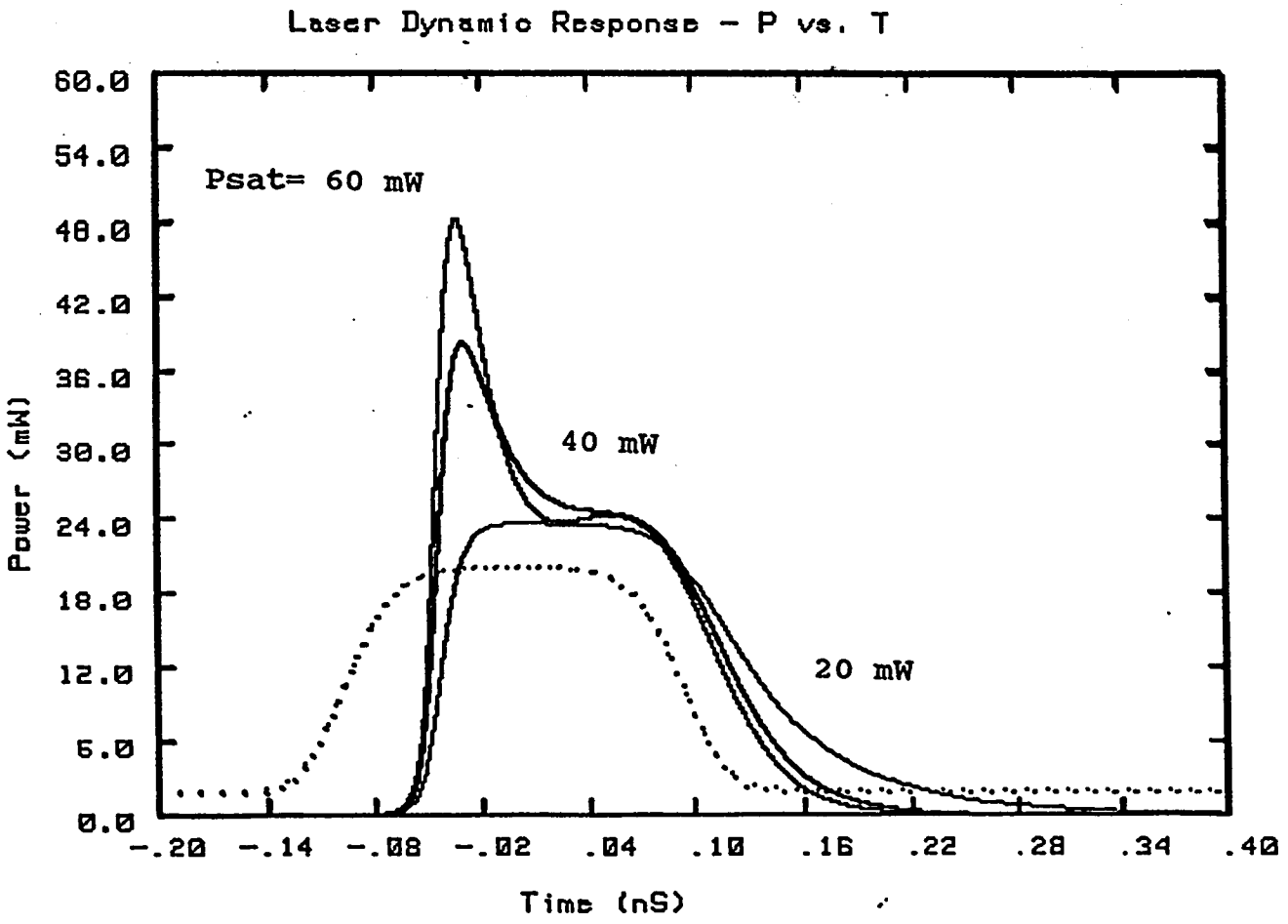

Figure 5. Facet output power versus time (Super-gaussian pulse, varying P_{sat}, 5 Gbit)

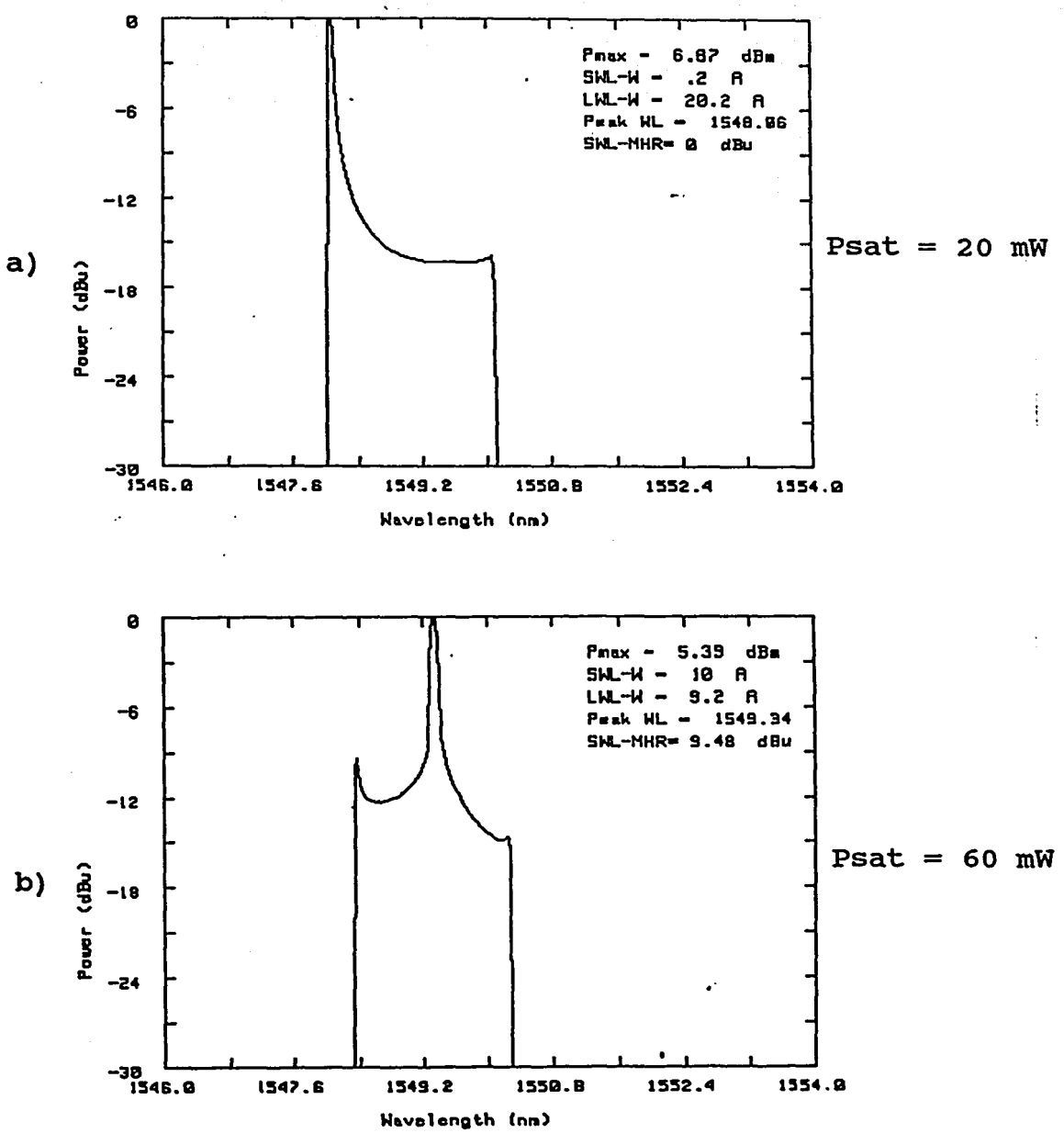

Figure 6. Optical intensity versus wavelength (Super-gaussian pulse, varying P_{sat}, 5 Gbit)

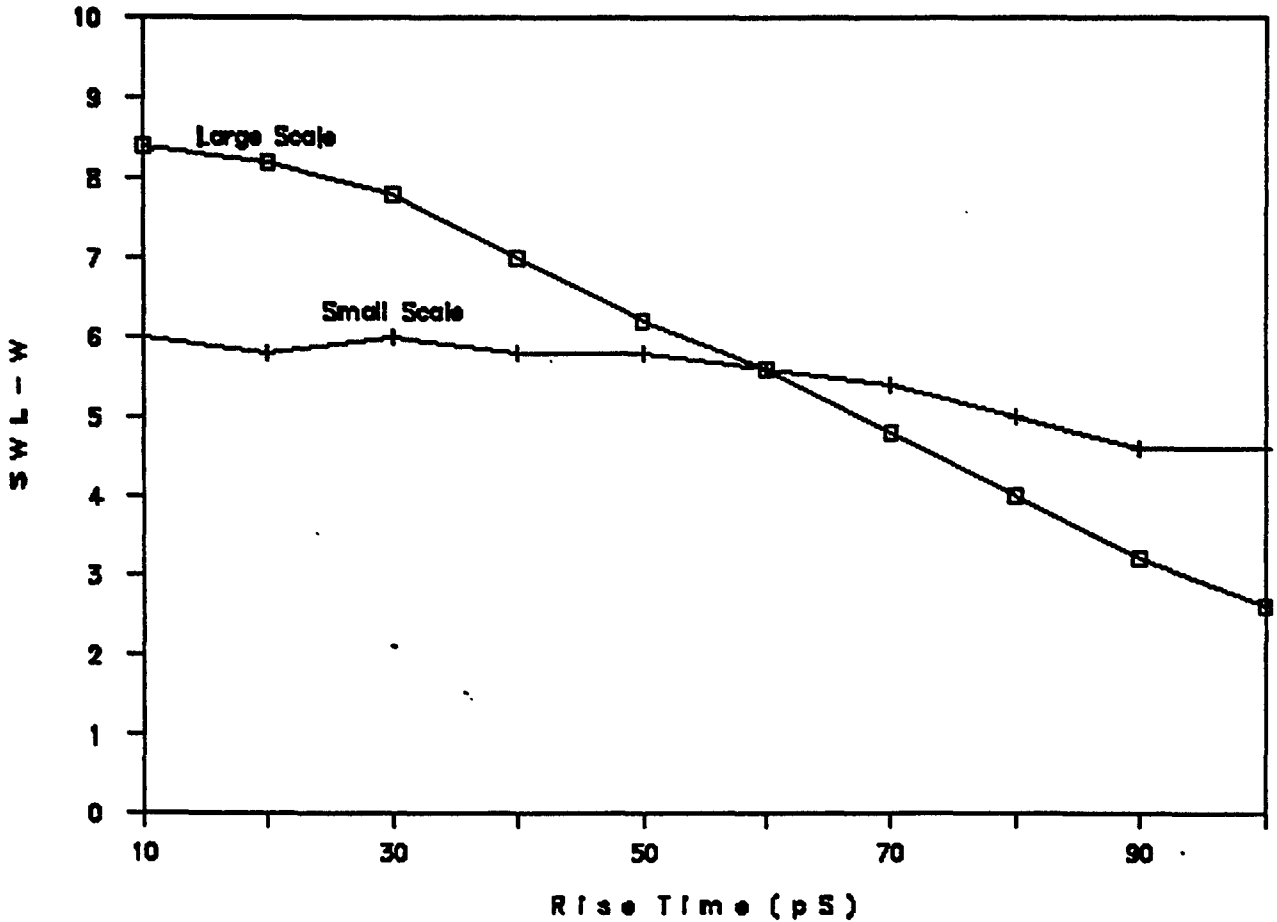

Figure 7. SWL-W versus normal and large scale modulation at 2 Gbit as a function of pulse rise time

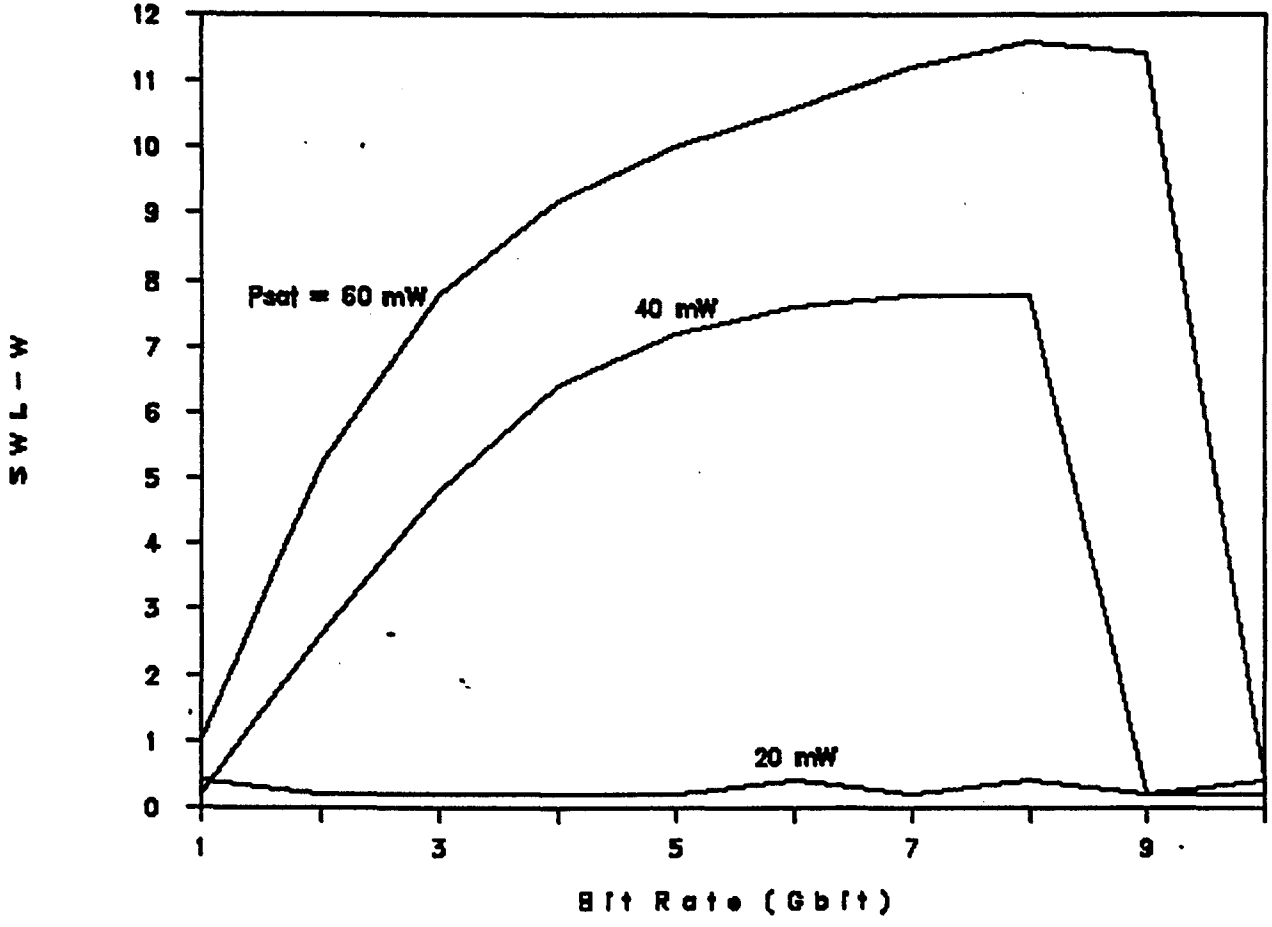

Figure 8. SWL-W for varying P_{sat} versus modulation rate

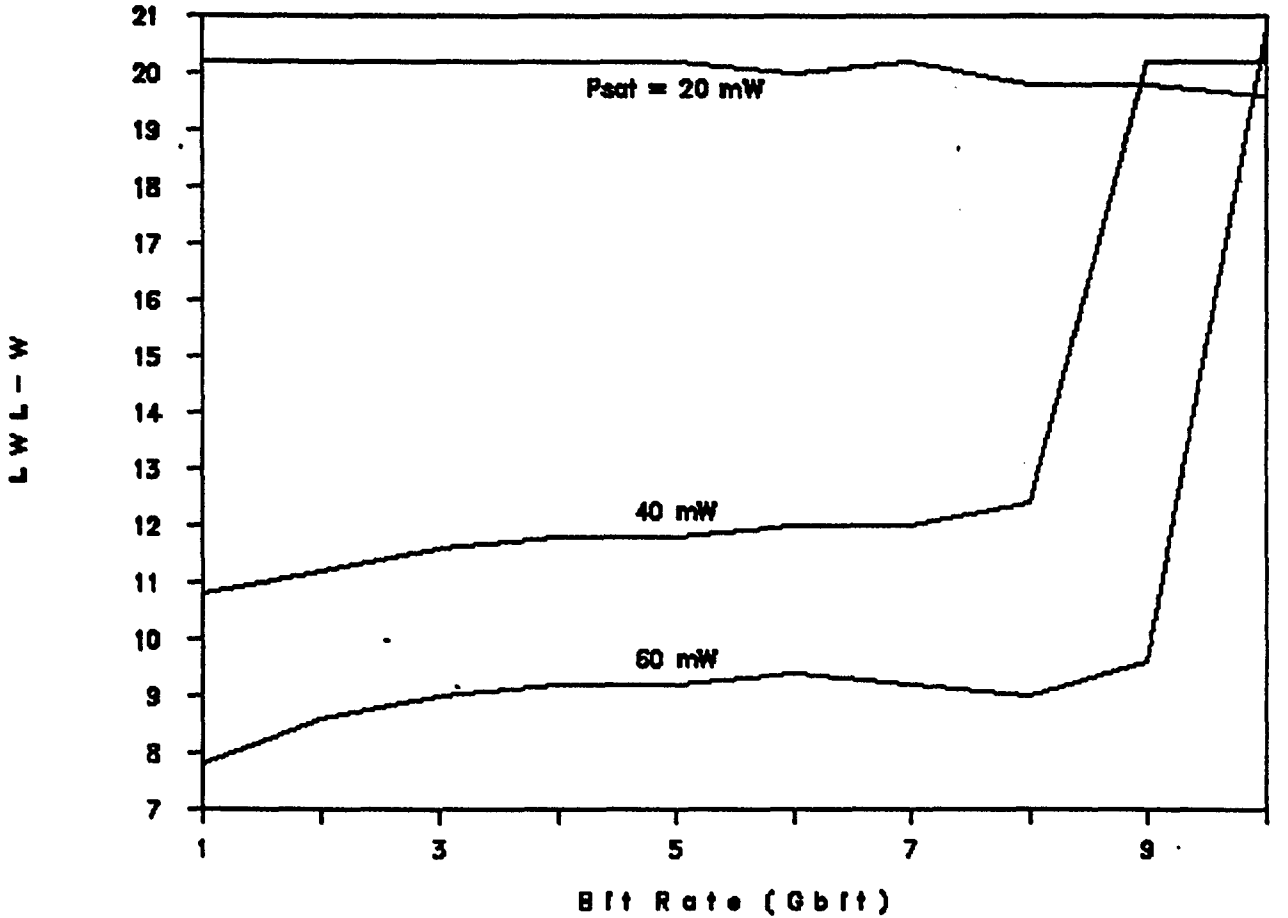

Figure 9. LWL-W for varying P_{sat} versus modulation rate

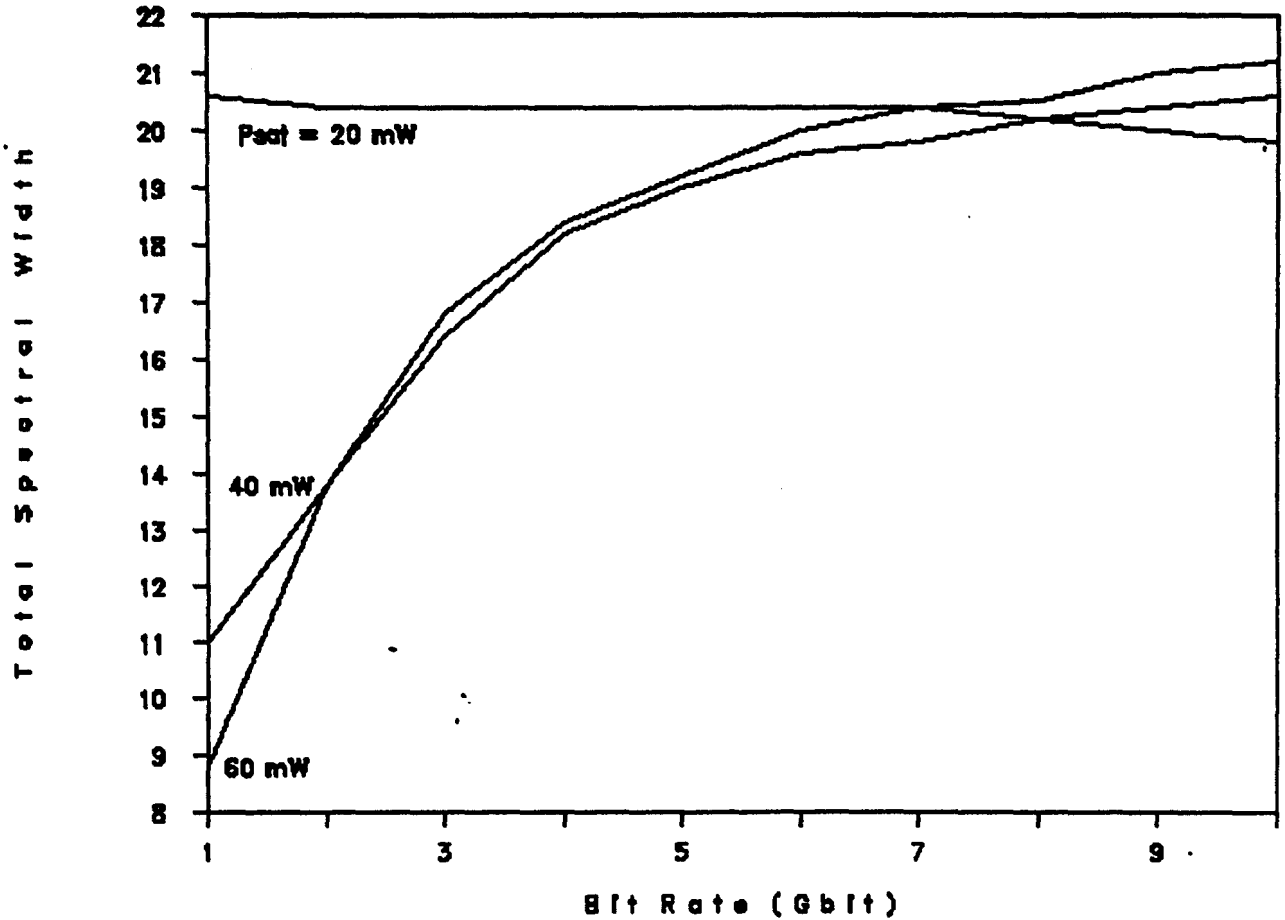

Figure 10. Total spectral width for varying P_{sat} versus modulation rate

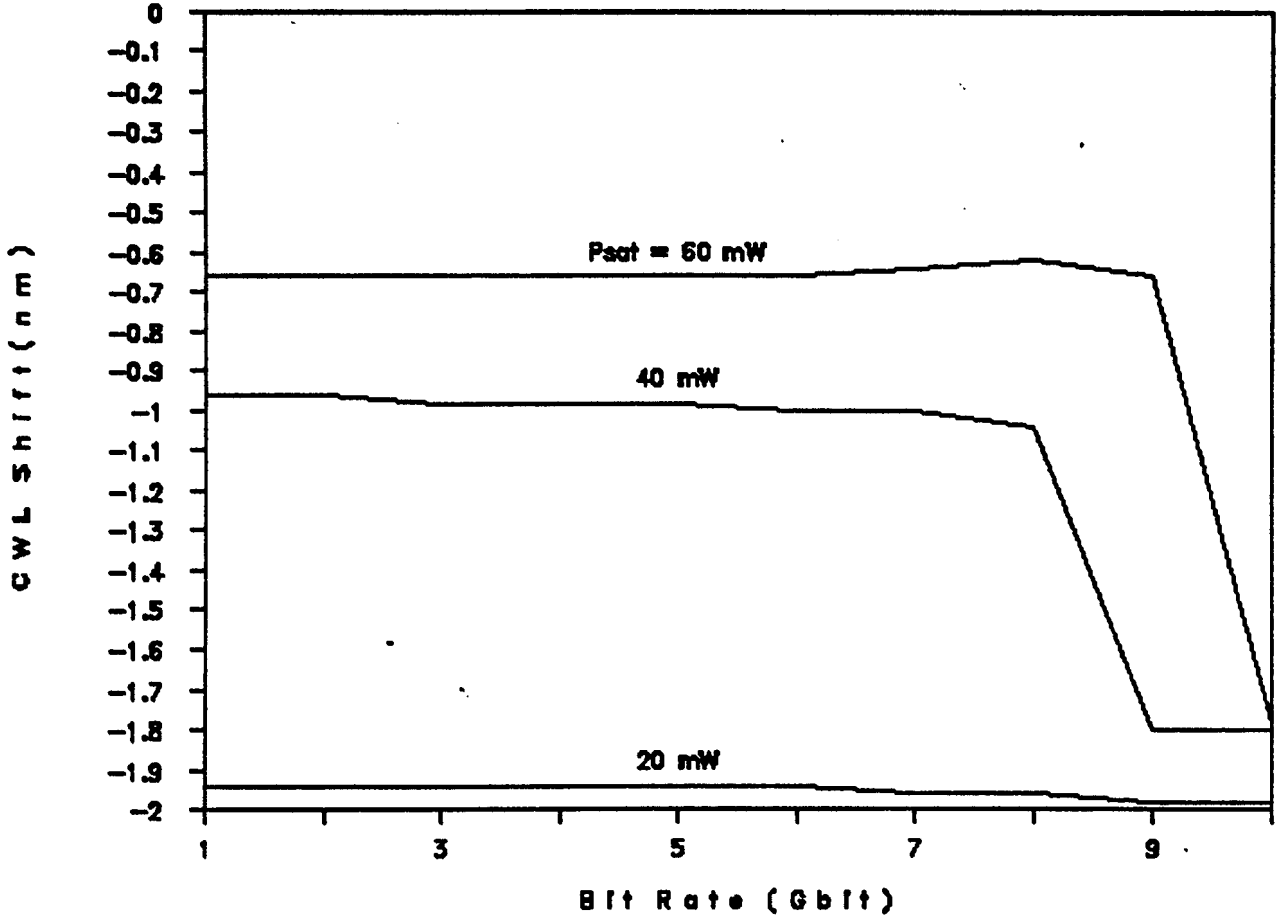

Figure 11. Center wavelength shift for varying P_{sat} versus modulation rate

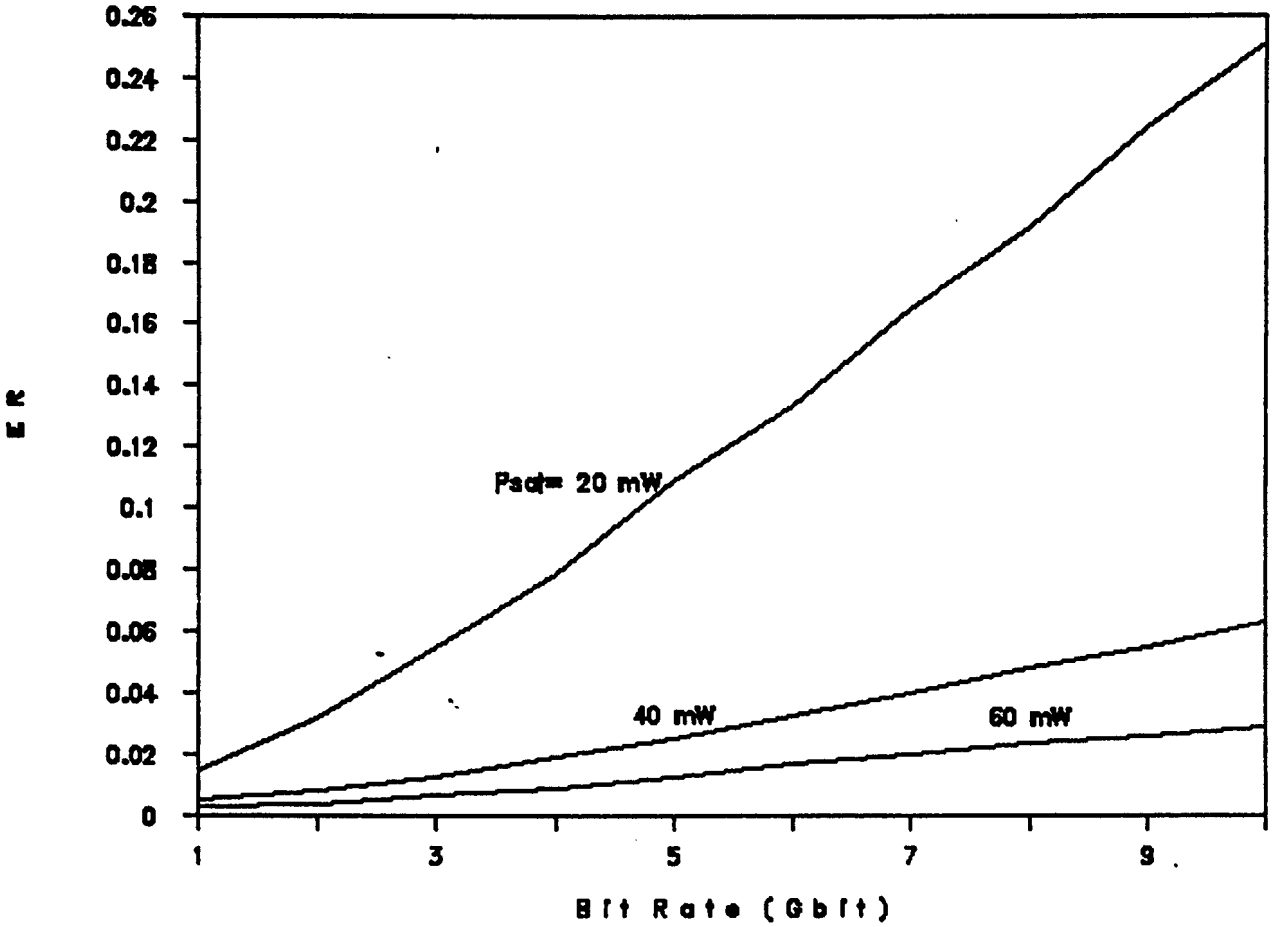

Figure 12. ER for varying P_{sat} versus modulation rate for $T_r = 0.1 * T_b$

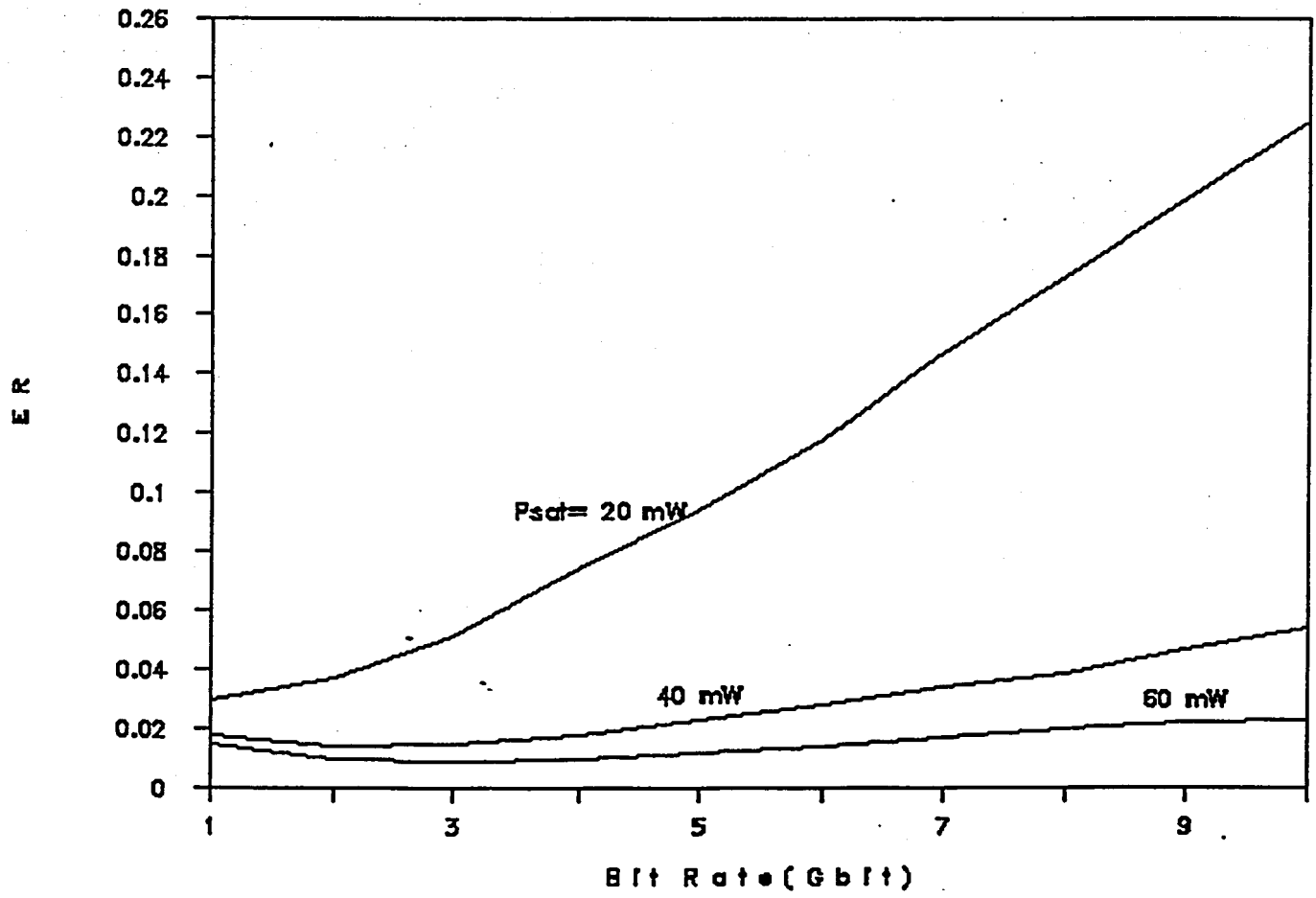

Figure 13. ER for varying P_{sat} versus modulation rate for $T_r = 0.2*T_b$

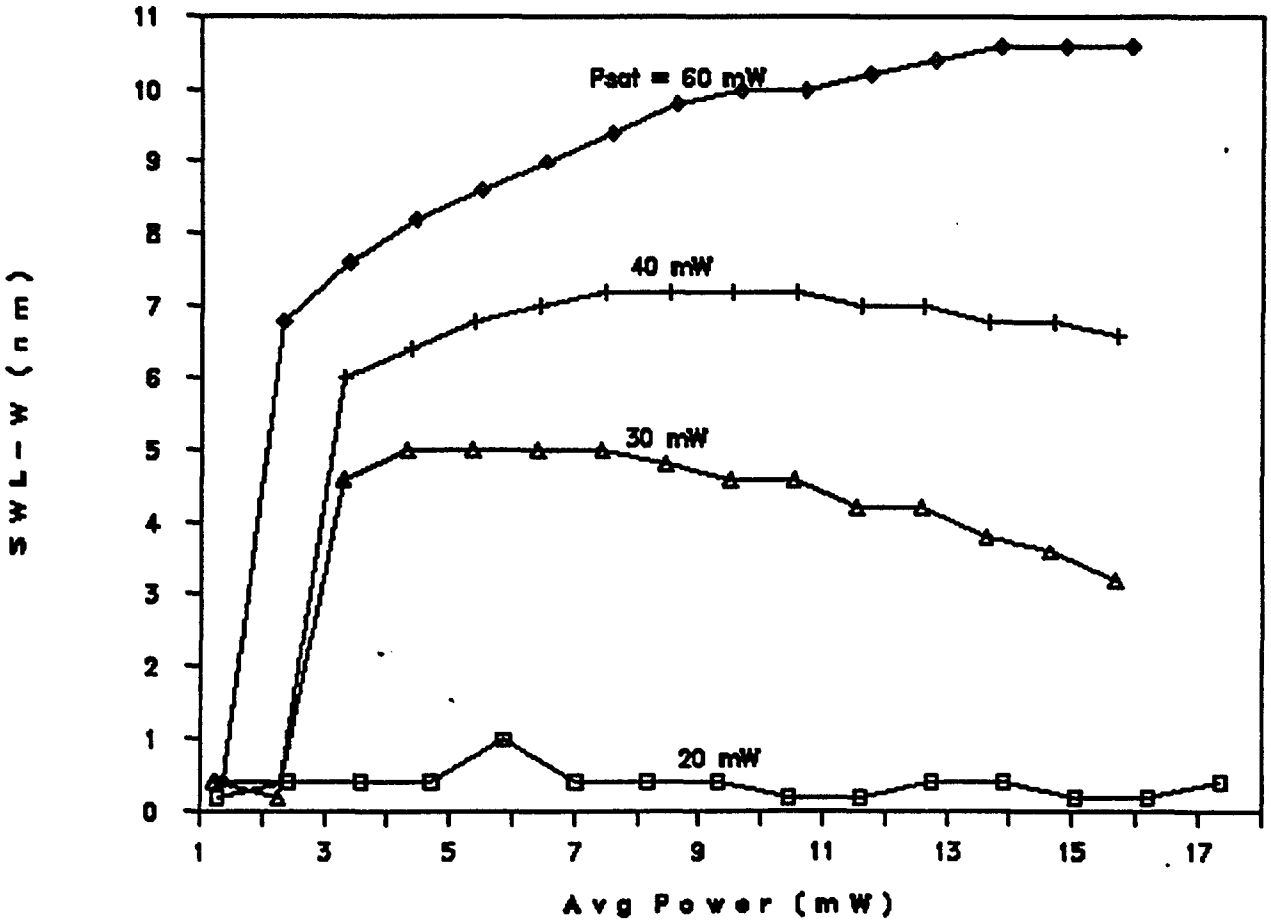

Figure 14. SWL-W versus average optical output power at 5 Gbit

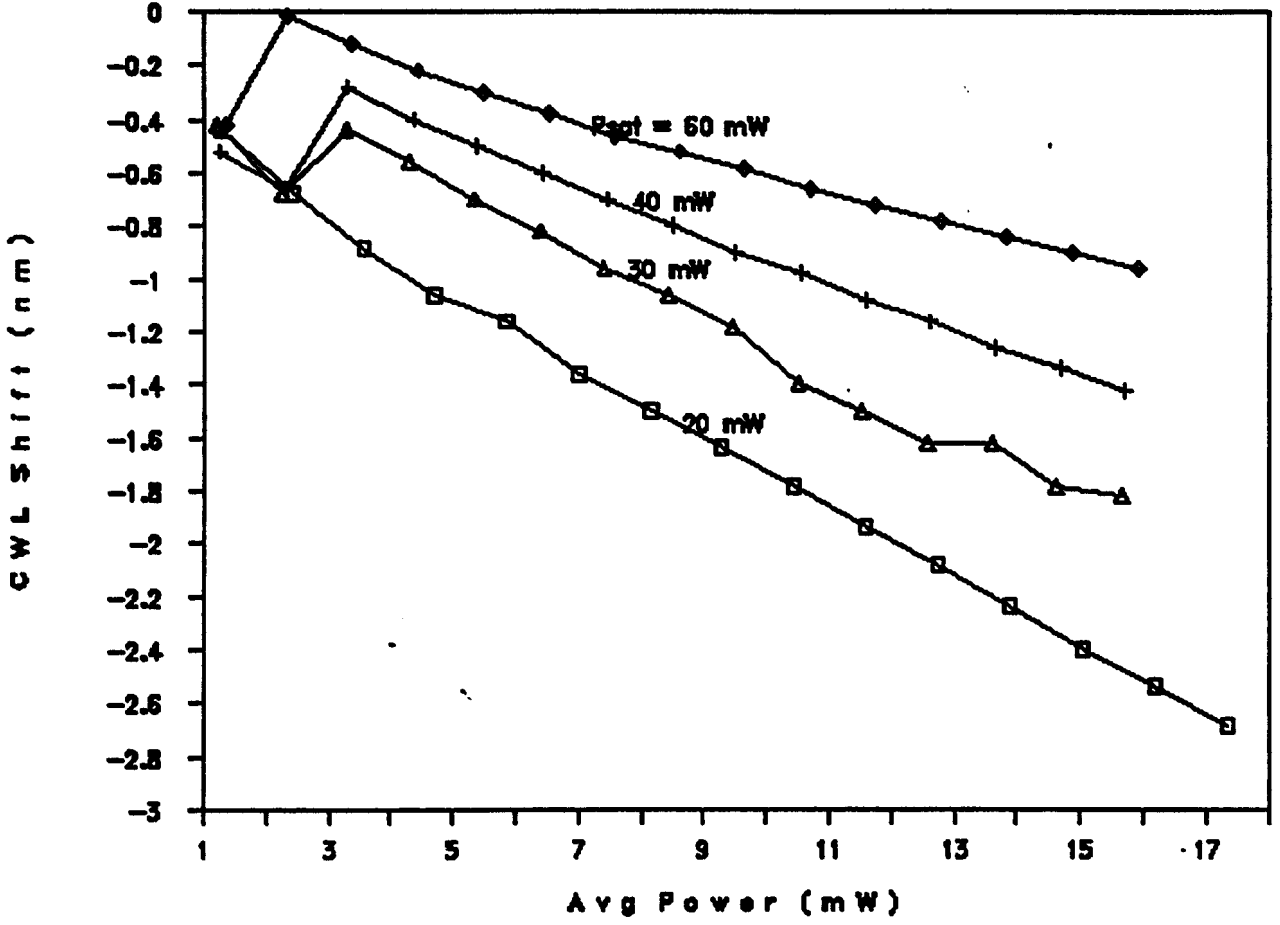

Figure 15. CWL versus average optical output at 5 Gbit

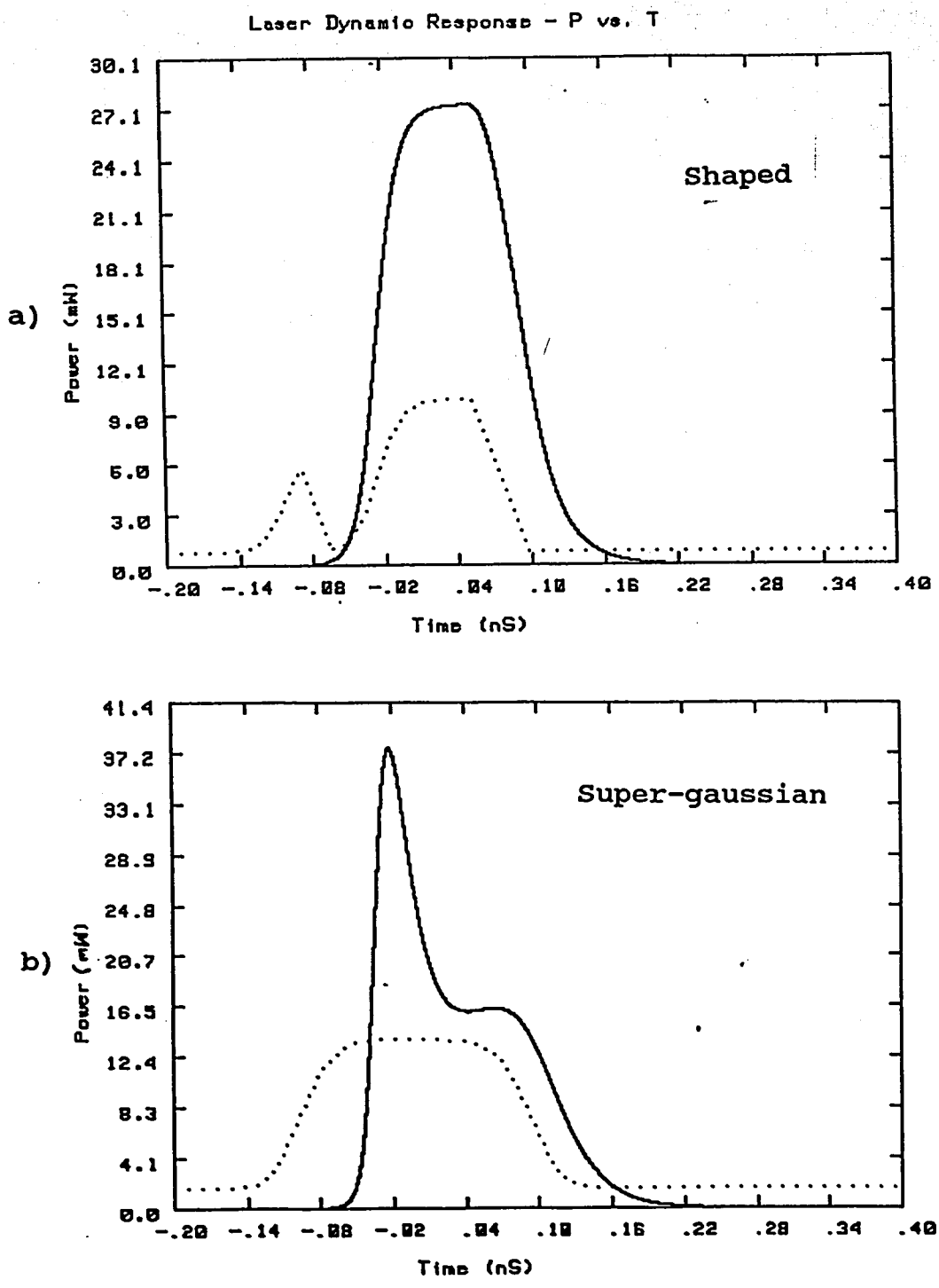

Figure 16. Power output versus time for shaped and super-gaussian current impulses at 5 Gbit

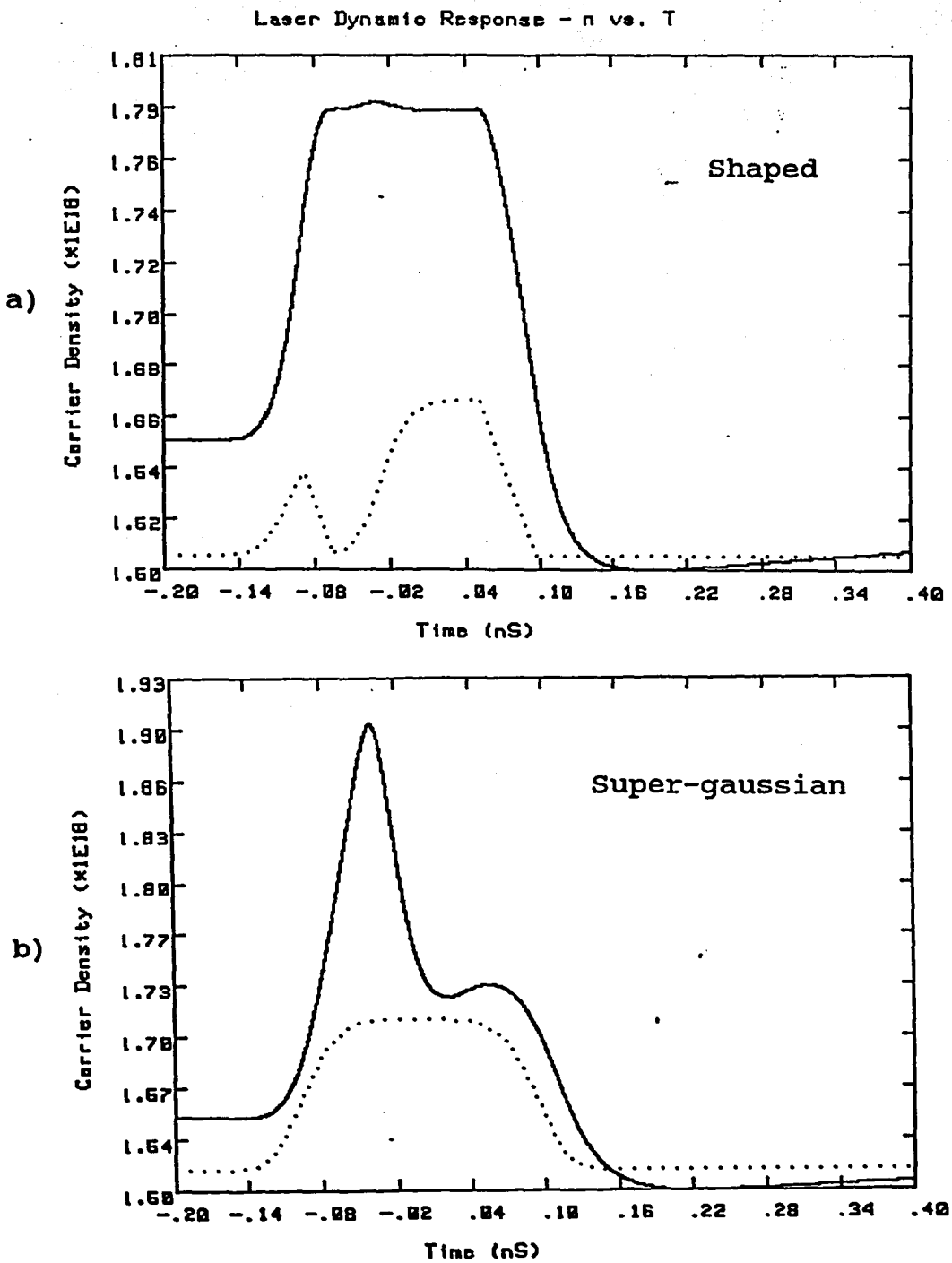

Figure 17. Carrier density versus time for shaped and super-gaussian impulses at 5 Gbit

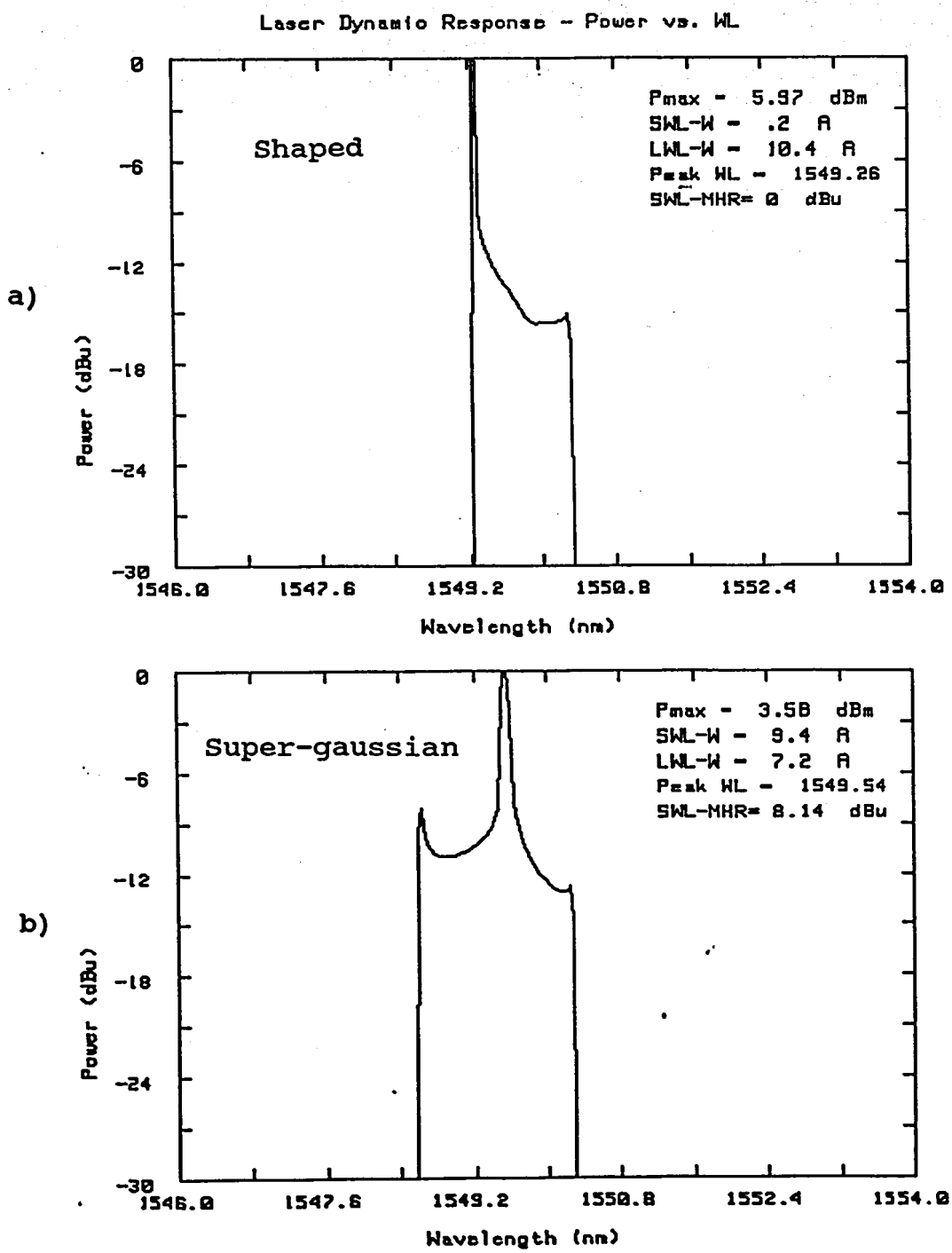

Figure 18. Optical intensity versus wavelength for shaped and super-gaussian impulses at 5 Gbit

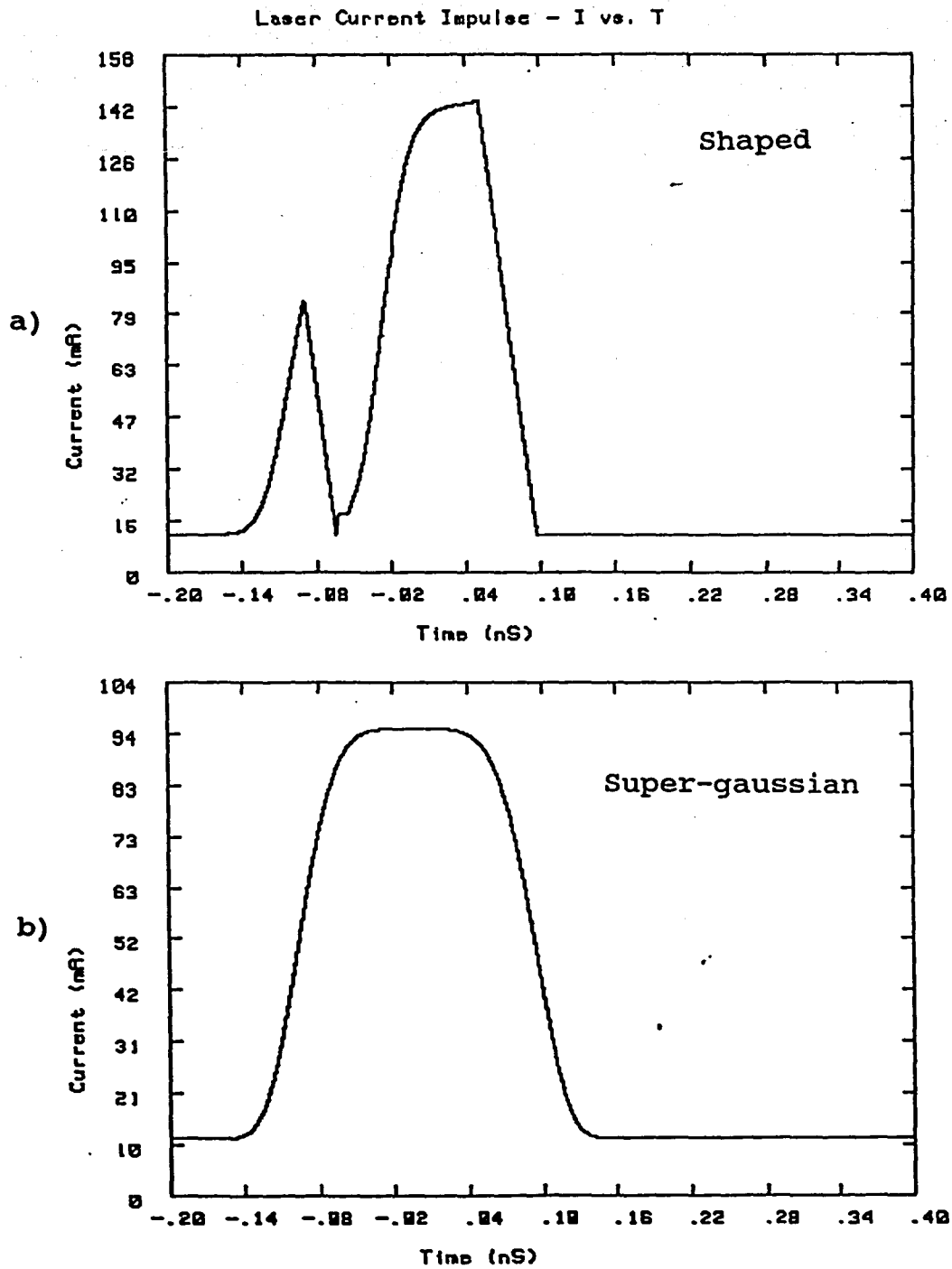

Figure 19. Modulation current versus time for shaped and super-gaussian modeling at 5 Gbit

a)

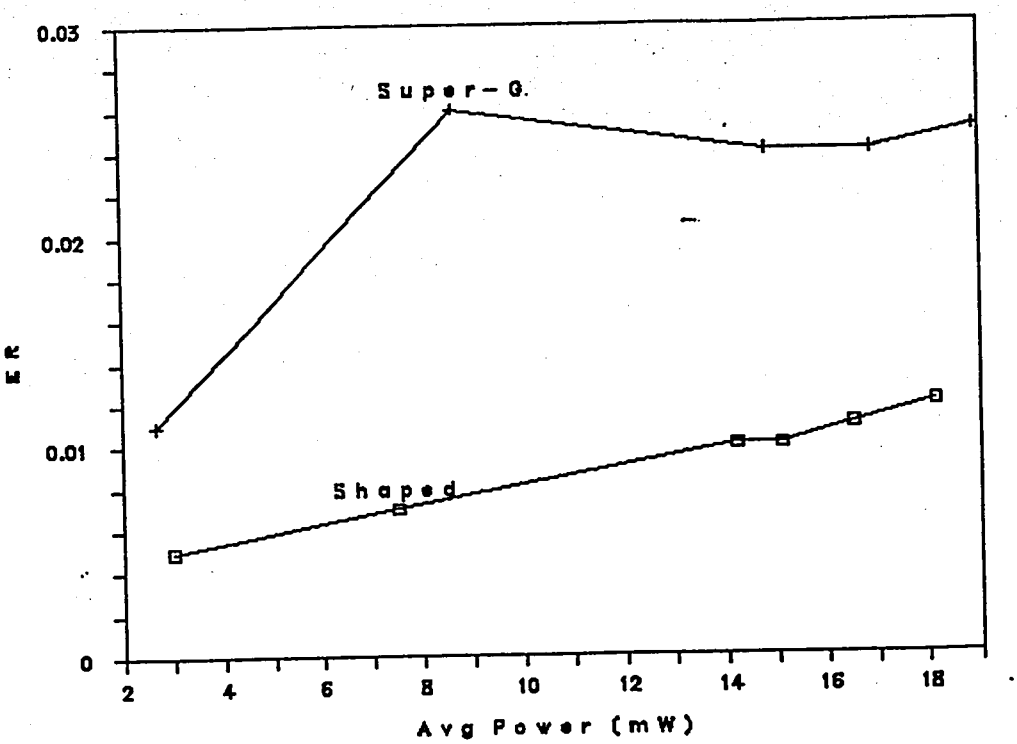

b)

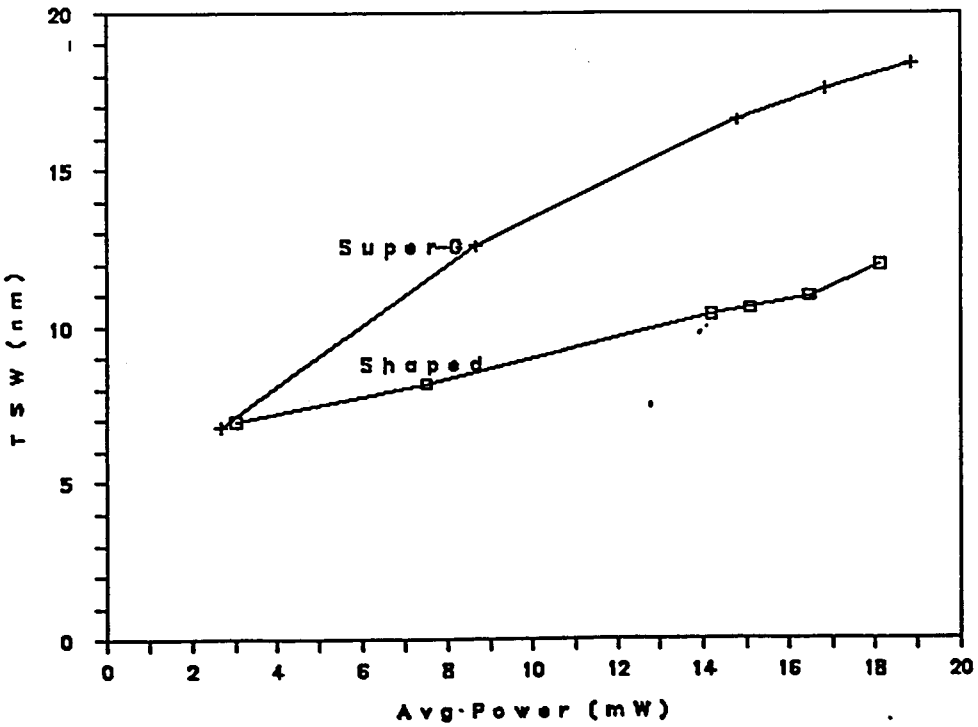

Figure 20. ER and total spectral width versus average power for shaped and super-gaussian current impulses at 5 Gbit

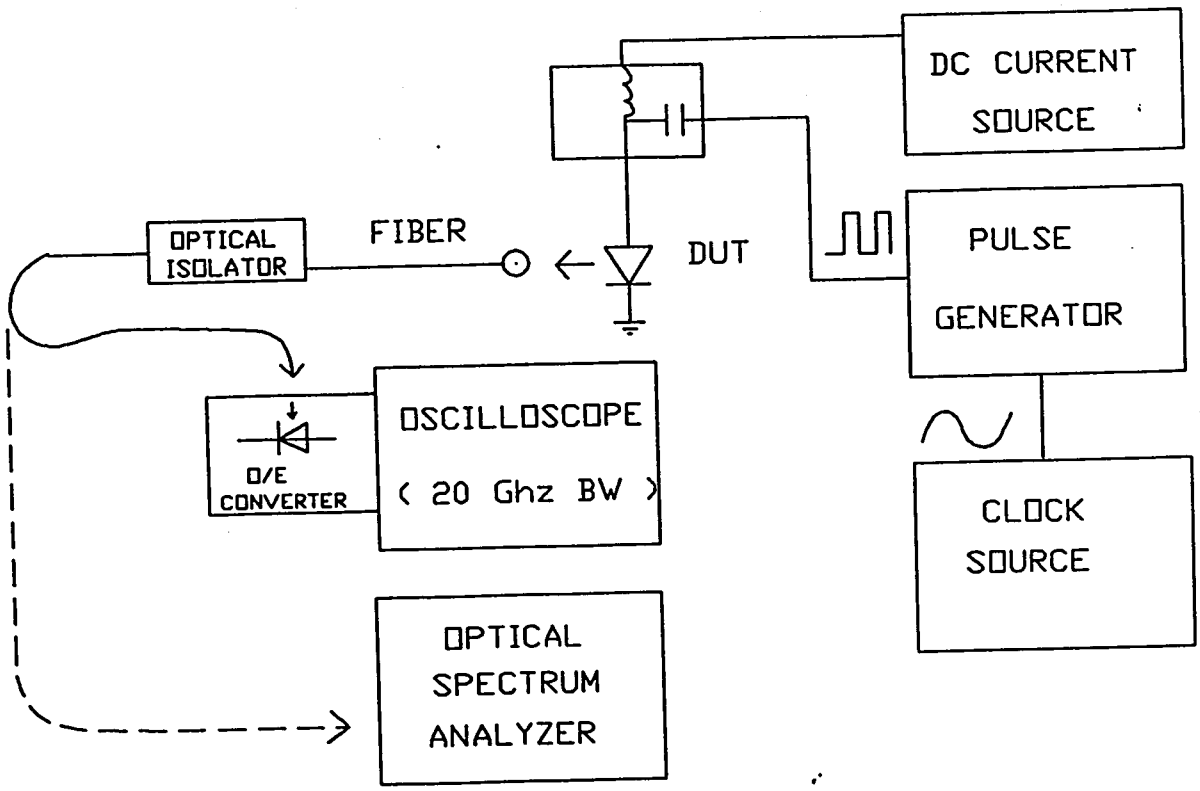

Figure 21. Experimental setup for wavelength chirp and optical pulse measurements

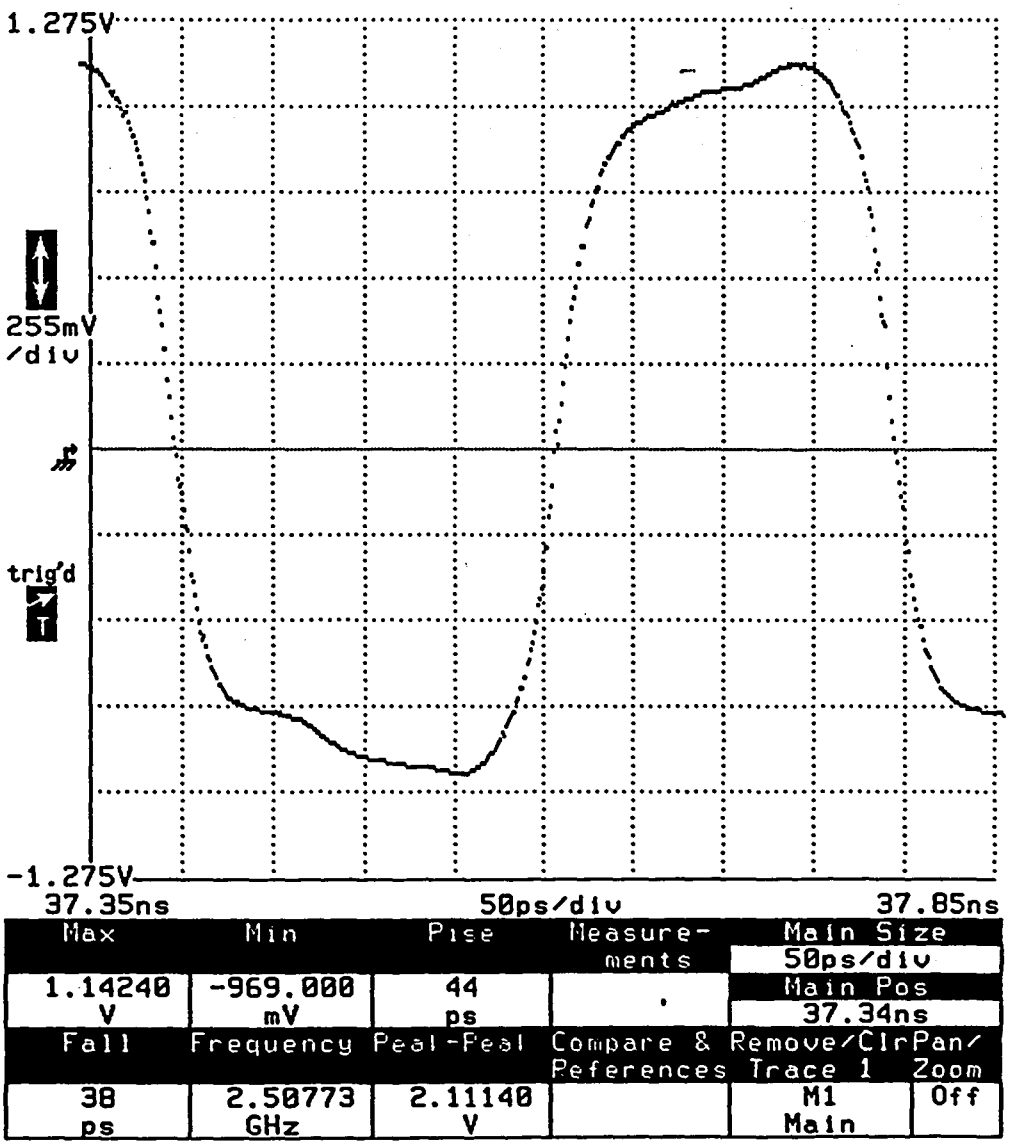

Imod = 40 mA

Figure 22. Modulation current waveform at 5 Gbit

DUT 1

DUT 2

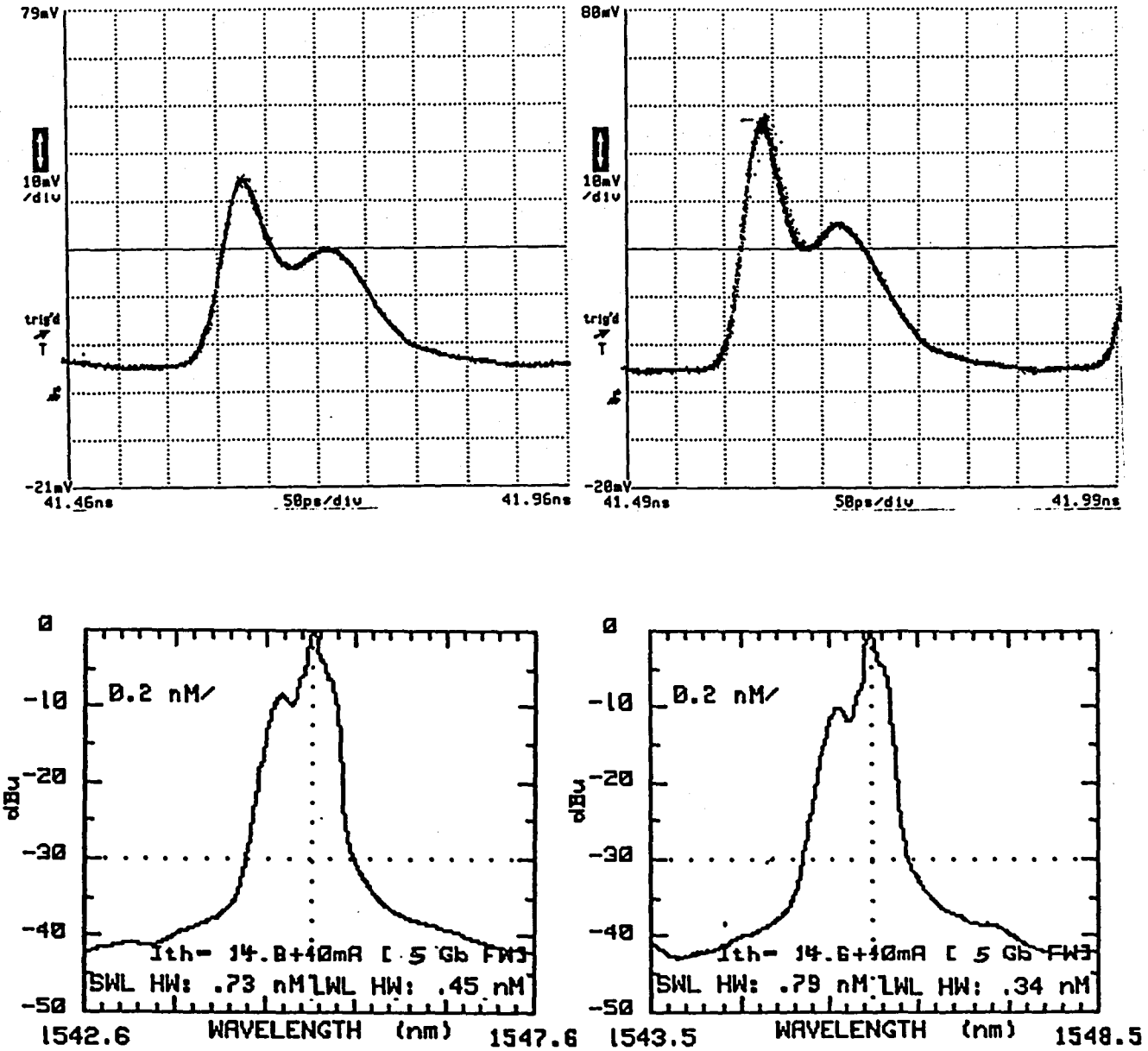

Imod = 40 mA

Figure 23. Experimental DFB laser response at 5 Gbit and normal scale modulation current.

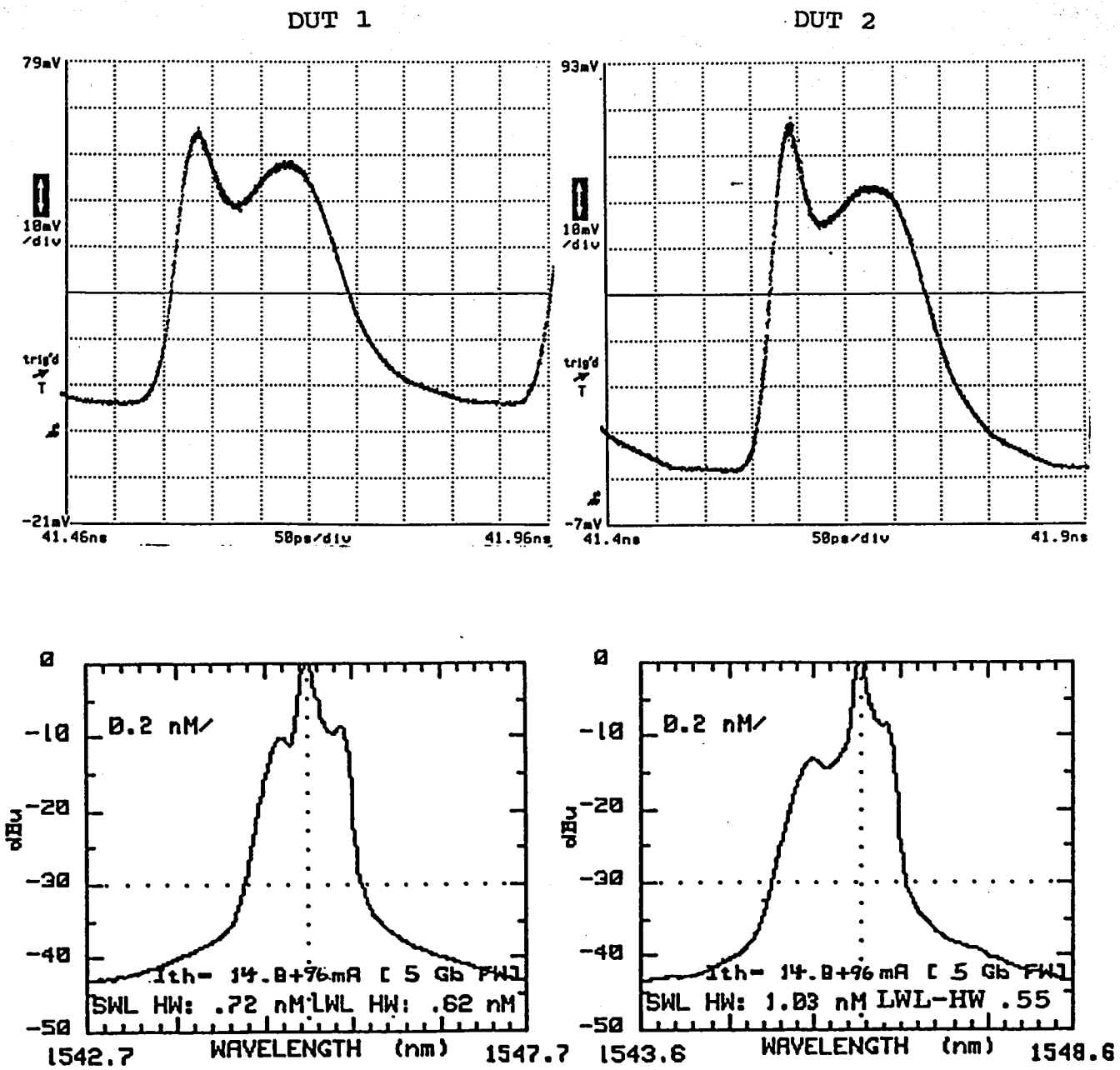

Imod = 96 mA

Figure 24. Experimental DFB laser response at 5 Gbit and large scale modulation current

BIBLIOGRAPHY

[1] Agrawal, G. P., "Spectral Hole-burning and Gain Saturation in Semiconductor Lasers: Strong Signal Theory" J. Applied Physics, Vol. 63 (1988), pp. 1232-1235

[2] Yariv, A. Optical Electronics. New York: Holt , 1985

[3] Chow, W. W., Dente, G. C., Depatie, D., "Saturation Effects in Seemiconductor Lasers" IEEE Journal of Quantum Electronics, Vol. 23 (1987) p. 1314-1320

[4] Agrawal, G. P., "Fundamental Limitation on Large-Signal Modulation of Semiconductor Lasers and its Implications for Lightwave Transmissions" Electronics Letters, Vol. 26 (1990), pp. 916-918

[5] Agrawal, G. P., Dutta, N. K. Long-Wavelength Semiconductor Lasers. New York: Van Nostrand Reinhold Co. , 1986

[6] Maron, Melvin J. Numerical Analysis. New York: Macmillan Co. , 1982

[7] Henry, Charles H., "Performance of Distributed Feedback Lasers Designed to Favor the Energy Gap Mode", IEEE Journal of Quantum Electronics, Vol QE-21 (1985), pp. 1913-1918

[8] Kinoshita, J and Matsumoto, K., "Transient Chirping in Distributed Feedback Lasers: Effect of Spatial Hole-Burning Along the Laser Axis", IEEE Journal of Quantum Electronics, Vol. 24 (1988) pp. 2160-2169

[9] Whiteaway, James E. A., Thompson, G. H. B., Collar, Andrew J., Armistead, Christopher J., "The Design and Assessment of 1/4 Phase-Shifted DFB Laser Structures", IEEE Journal of Quantum Electronics, Vol. 25 (1989), pp. 1261-1279

[10] Koch, T. L. and Linke, R. A., "Effect of Nonlinear Gain Reduction on Semiconductor Laser Wavelength Chirping", Applied Physics Letters, Vol. 48 (1986) pp. 613-615

[11] Henry, C. H., "Theory of the Linewidth of Semiconductor Lasers", IEEE Journal of Quantum Electronics, Vol. QE-18 (1982) pp. 259-264

[12] Olshansky, R. and Fye, D., "Reduction of Dynamic Linewidth in Single-Frequency Semiconductor Lasers", Electronic Letters, Vol. 20 (1984) pp. 928-929

VITA

The author was born in Hartford, Connecticut on March 15, 1962. His parents are Adele and Francis Strelchun. He attended the University of Scranton, Scranton, Pennsylvania from September 1979 to May 1983 and achieved a Bachelor of Science degree in Electronics Engineering with Cum Laude honors. The author began a Master of Science degree in Electrical Engineering at Pennsylvania State University in 1984. He transferred to Lehigh University in the Fall of 1986 and subsequently completed the Master of Science degree program.

The author has been employed at A.T & T. Micro-electronics in Reading, Pennsylvania since June of 1983. He is currently an MTS (Member of Technical Staff) and is involved with the design and development of semiconductor laser test equipment. The tested laser components are used in high speed telecommunications systems.

END

OF

TITLE